J. Fluid Mech. (1971), *vol.* 50, *part* 4, *pp.* 751–783
Printed in Great Britain

The spacing, position and strength of vortices in the wake of slender cylindrical bodies at large incidence

By K. D. THOMSON AND D. F. MORRISON†
Weapons Research Establishment, Salisbury, South Australia

(Received 30 May 1970 and in revised form 14 June 1971)

Extensive schlieren studies and yawmeter traverses of the wake behind slender cone-cylinders at large angles of incidence have shown that the flow pattern is generally steady. Under certain flow conditions, however, the wake exhibits an instability which is not understood. For cross-flow Reynolds numbers in the subcritical region the wake can be described in terms of a cross-flow Strouhal number which has a constant value of 0·2 for cross-flow Mach number components (M_c) up to 0·7 and then increases steadily to a value of 0·6 at $M_c = 1{\cdot}6$. The strength of the wake vortices varies substantially with M_c, increasing to a maximum at $M_c \approx 0{\cdot}7$ and then decreasing rapidly for higher values of M_c. Schlieren photographs of the wake have been analysed by means of the impulse flow analogy and also by considering the vortices to be part of a yawed infinite vortex street. The impulse flow analogy is shown to be of use in determining the cross-flow Strouhal number but estimates of vortex strength are too high. The Kármán vortex street theory combined with the sweepback principle leads to reliable estimates of vortex strength up to $M_c = 1{\cdot}0$.

Information is given on the spacing, path and strength of the vortices shed from the body for flow conditions varying from incompressible speeds up to $M_c = 1{\cdot}0$. Finally this information is used to determine the vortex drag of a two-dimensional circular cylinder below $M_c = 1{\cdot}0$.

1. Introduction

Investigations of the behaviour of the flow over slender cylindrical bodies at incidence have been reported in numerous papers (see, for example, the list of references cited by Sarpkaya (1966) and the papers of Allen & Perkins (1951), Bursnall & Loftin (1951), Hall, Rogers & Davis (1959), Jorgensen & Perkins (1958), Maltby & Peckham (1956) and Thomson & Morrison (1965)). Many of these investigations have been based on the so-called impulse flow analogy which has been well described by Allen & Perkins (1951) and more recently investigated by Sarpkaya (1966). According to the analogy the progressive development of the wake along the body when viewed in cross-flow planes is similar to the growth with time of the flow behind a two-dimensional cylinder started impulsively from rest. Close to the body nose no wake exists whereas further downstream two symmetrically disposed vortices form on the lee side.

† Deceased.

These vortices are fed by vortex sheets containing boundary-layer fluid which has separated from the body. Further along the body first one and then the other of these vortices detaches and moves downstream at an angle to the free stream. Other vortices form on the lee side of the body at increasing distance and behave in a similar manner. This process continues along the body length and a flow cross-section taken at right angles to the axis far from the nose has the appearance of a vortex street. The flow pattern is depicted in figure 1 and resembles a space–time plot of the flow past a two-dimensional cylinder started impulsively from rest.

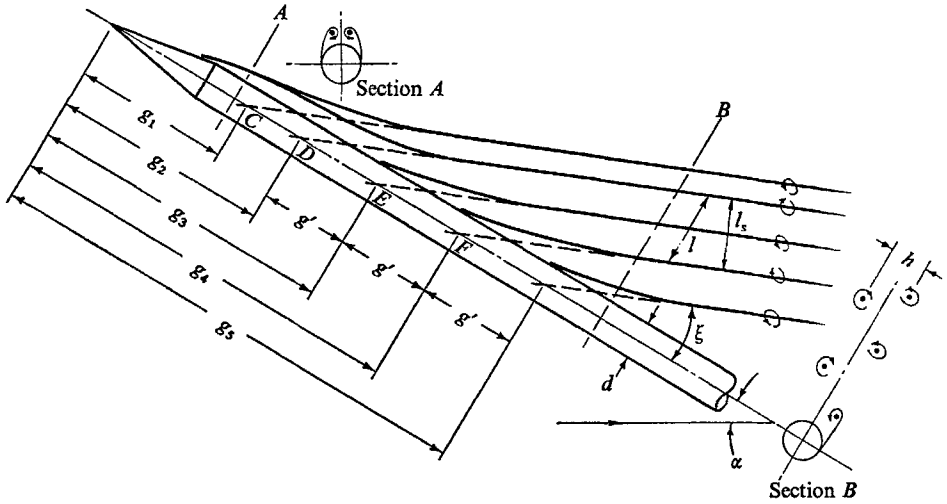

FIGURE 1. Sketch of wake from slender cone-cylinder at large incidence.

This pattern, which is steady, prevails over a substantial range of incidence. However, at very high angles there is a change to an unsteady flow régime in which the vortex lines become parallel to the body. The flow pattern then appears similar to that past a two-dimensional cylinder with both the cylinder and wake rotated through the same angle of yaw. The change-over from one type of pattern to the other is illustrated in Fiechter's (1966) beautiful colour photographs of the low-speed flow over an ogive cylinder; in this particular case the change over occurred at an incidence of approximately 60°. The major part of the investigations reported herein refer to the steady flow régime depicted in figure 1.

Many of the investigations (e.g. Jorgensen & Perkins 1958; Mello 1959) reported to date have been concerned with bodies at moderate angles of incidence, for which the symmetrical wake configuration is predominant (section *A* in figure 1). At large angles of incidence this shrinks towards the nose and the asymmetric flow pattern (section *B* in figure 1) becomes very extensive. The latter case has been examined by Fiechter (1966) and in more detail by the present authors (1965) who proposed a method based on a combination of Kármán's vortex street theory and the impulse flow analogy for describing the asymmetrical wake pattern in incompressible flow. According to this method the angle between the body centre-line and the paths traced by the shed vortices can be used

to determine the vortex strength, while the spacing of the vortex paths is a measure of the Strouhal number of the wake from a circular cylinder with identical cross-flow conditions. The method, however, could not account for compressibility effects. Further experiments were therefore conducted to measure the cross-flow Strouhal number, vortex strength and vortex starting positions in the wake from slender cone-cylinders at incidence over a wide range of flow conditions in order to investigate compressibility effects in some detail.

Results of this experiments have been reported by the authors (1969) who analysed the data on the basis of the impulse flow analogy. Subsequently Professor M. V. Morkovin pointed out (private communication) that the vortices in the wake (figure 1, for example) should behave as a yawed vortex street and that it should be possible to examine them using the sweepback principle and vortex street theory, without recourse to the impulse flow analogy. This in turn should lead to an assessment of the errors arising from use of the impulse flow analogy. In the light of this suggestion the information in the authors' (1969) report has been re-analysed and is presented herein.

Allen & Perkins (1951) found that the vortex paths could be made visible by the use of a standard schlieren system, and a substantial part of this paper is concerned with measurements taken from schlieren photographs. However, results from several other experiments are included. In order to verify that measurements made from the schlieren photographs gave an accurate estimate of the cross-flow Strouhal number when compressibility effects were significant, a two-dimensional unyawed cylinder containing a piezo-electric transducer was used to measure the Strouhal number directly at cross-flow Mach numbers between 0·3 and 0·65. Since some authors (see, for example, Hall *et al.* 1959) had observed that the wake exhibited an unsteady behaviour which varied with nose geometry, the steadiness of the flow pattern behind a slender cone-cylinder was examined to give background information to the schlieren studies. In a further experiment Pitot and yawmeter traverses were made at several Mach numbers in the wake behind a number of cone-cylinders at 30° incidence. The Pitot pressure plots gave information on the growth of the wake vortices and the results of the yawmeter traverses were used to obtain the strength of the vortices for comparison with the values deduced from the schlieren photographs. Finally, reference is made to an experiment conducted by Griss (1967) on the wake from an ogive cylinder at a speed of 100 ft/sec. This experiment gave information on the vortex strength in the incompressible speed range.

2. Theoretical considerations

A sketch of the vortex system behind a slender cone-cylinder at incidence is shown in figure 1. The flow pattern will be analysed in two ways, first by using the impulse flow analogy according to which the flow is unsteady in a direction normal to the body axis and secondly by considering the vortex pattern as a steady yawed vortex street, for which the sweepback principle holds. In both cases Kármán's vortex street theory will be used and this immediately places certain restrictions on the applicability of the method.

In the first place, for Kármán's theory to hold, an infinite vortex street is required and all vortices must have the same strength. These conditions are not met in the flow over a body at incidence in that only a few vortices may be present and these need not all have the same strength. Each vortex contains boundary-layer fluid which was initially located along a well-defined section of the body surface (see figure 1) and it is the circulation generated in this boundary layer which determines the strength of the vortex. Hence vortices will only have the same strength when the boundary-layer behaviour is the same on each body section, and this is true only when the nose ceases to influence the body pressure distribution. Generally the nose influence extends a few diameters downstream of the cone-cylinder junction and any vortices which are generated from the boundary-layer upstream of this region will have different strengths from those generated downstream. The first two vortices contain boundary-layer fluid from the nose and cannot strictly be considered as part of a Kármán vortex street. The third vortex is likely to contain boundary fluid which was originally on the body downstream of the cone-cylinder junction. It is therefore more representative of the vortices following and, even though some nose influence may be present, the third vortex could possibly be considered as the first 'genuine' vortex of the equivalent Kármán vortex street after it moves away from the immediate influence of the cylinder and its path becomes straight.

The second restriction is that Kármán's vortex street theory holds for incompressible flow and its present extension to higher speeds where compressibility effects are significant may be expected to lead to errors.

2.1. *Impulse flow analogy*

The basic parameter for describing the periodic shedding of vortices from a circular cylinder in two dimensions is the Strouhal number S which is defined as

$$S = nd/U,$$

where n is the frequency (in Hz) of shedding of vortices of like sign, d is the diameter of the cylinder and U is the velocity of the cylinder relative to the free stream.

If we now consider a cylinder at an angle α to a free stream with velocity V, the velocity at right angles to the cylinder is

$$U = V \sin\alpha,$$

and hence

$$S = nd/V \sin\alpha,$$

or

$$1/n = d/SV \sin\alpha.$$

Now $1/n$ represents the time interval between the instants of shedding of vortices of like sign and it also represents the time taken for the component of flow along the body centre-line, $V\cos\alpha$, to traverse a distance $2g'$ as shown in figure 1.

Thus

$$1/n = d/SV \sin\alpha = 2g'/V\cos\alpha,$$

or

$$S = 1/2(g'/d)\tan\alpha. \tag{1}$$

The equivalent two-dimensional Strouhal number for the wake vortex system behind a cone-cylinder at incidence can thus be calculated purely from the geometry of the wake.

Kármán's vortex street theory (e.g. Durand 1935) is now used to find the strength of the vortices as follows. A cylinder moving at speed U leaves behind it a wake which moves at a speed U_2, i.e. the speed of the wake relative to the cylinder is $U(1-U_2/U)$. Kármán has shown that

$$U_2/U = \tfrac{1}{2}(\Gamma_1/Ud)\,(d/l)\tanh(\pi h/l), \tag{2}$$

where Γ_1 is the vortex strength given by the impulse flow analogy, l is the distance apart of vortices of like sign, and h is the distance apart of the vortex rows. The angle between the vortex lines and the centre-line is ξ, where

$$\tan\xi = U(1-U_2/U)/V\cos\alpha,$$

or, putting $U = V\sin\alpha$, $$U_2/U = 1-\chi, \tag{3}$$

where $$\chi = \tan\xi/\tan\alpha.$$

Hence from a photograph of the wake, ξ and α can be measured and U_2 can be determined. Before Γ_1/Ud can be found from (2) it is necessary to determine d/l. Referring again to figure 1,

$$\frac{d}{l} = \frac{d}{2g'}\frac{2g'}{l} = \frac{d}{2g'}\cot\xi$$

and from equation (1), $2g'/d = 1/S\tan\alpha$. Therefore

$$d/l = S\tan\alpha/\tan\xi = S/\chi. \tag{4}$$

Equations (2)–(4) can be combined to give finally

$$\begin{aligned}\Gamma_1/Ud = \Gamma_1/Vd\sin\alpha &= 2(l/d)\,(1-\chi)\coth(\pi h/l)\\ &= (2\chi(1-\chi)/S)\coth(\pi h/l).\end{aligned} \tag{5}$$

2.2. *Sweepback principle*

In this case the wake is considered to be part of a steady infinite vortex street and the induced motion normal to the vortex lines is examined. By vortex street theory U_s, the self-induced transport velocity of the vortex street normal to the vortex lines, is given by

$$U_s = (\Gamma_s/2l_s)\tanh(\pi h/l_s), \tag{6}$$

where Γ_s is the vortex strength given by the sweepback principle and l_s is the distance apart of vortices of like sign, measured normal to the vortex lines. From figure 1

$$l_s = l\cos\xi. \tag{7}$$

Since the vortex lines in figure 1 are stationary, U_s must be countered by the component of free-stream speed normal to the vortex lines, i.e.

$$U_s = V\sin(\alpha-\xi). \tag{8}$$

Thus from (6)–(8),

$$\Gamma_s/Vd\sin\alpha = 2(l/d)\,(\sin(\alpha-\xi)/\sin\alpha)\cos\xi\coth(\pi h/l\cos\xi)$$
$$= 2(l/d)\,(1-\chi)\cos^2\xi\coth(\pi h/l\cos\xi). \quad (9)$$

The vortex strength deduced using the impulse flow analogy is greater than that found from the sweepback principle, and in fact

$$\Gamma_1/\Gamma_s = \coth(\pi h/l)/\cos^2\xi\coth(\pi h/l\cos\xi). \quad (10)$$

It is apparent that, provided h/l can be determined, equations (5) and (9) can be evaluated from schlieren photographs of the wake. However, it is repeated that (1), (5) and (9) should only be used to interpret photographs of the wake when the cross-flow component of the free stream can be classed as incompressible. Nevertheless, these equations represent useful groupings of the wake parameters and it will be demonstrated later that they enable the wake behaviour to be correlated over a large range of Mach number and body incidence. The vortex spacing ratio h/l is discussed in § 4.5.

3. Experimental methods

Apart from the experiment conducted by Griss (1967) in a 9 ft × 7 ft wind tunnel, all tests were carried out in the 15 in. square continuous-flow high-speed tunnel at the Weapons Research Establishment. The cross-flow Reynolds number (defined as $R_c = Vd\sin\alpha/\nu$, ν being the kinematic viscosity) was less than or equal to $2{\cdot}3\times10^5$ for tests on the unyawed cylinder and $R_c \leqslant 7{\cdot}5\times10^4$ for all experiments on cone-cylinders at incidence. Work on yawed cylinders by Bursnall & Loftin (1951) showed that at values of cross-flow Mach number component M_c ($= M\sin\alpha$, M being the free-stream Mach number) less than 0·2 a subcritical type of flow separation is to be expected in this range of cross-flow Reynolds numbers. At higher speeds Gowen & Perkins (1953), and also Naumann, Morsbach & Kramer (1966), have shown that for two-dimensional unyawed cylinders at subsonic speeds the effect of increasing Mach number is to move forward the points of flow separation at subcritical Reynolds numbers. On this basis and from observations during experiments it is concluded that in all tests subcritical flow separations occurred.

The experimental methods described below are not given here in great detail; additional information may be obtained from Thomson & Morrison (1969).

3.1. *Schlieren studies*

Allen & Perkins (1951) found that a vortex line becomes visible when viewed in a schlieren system. The image of such a vortex line appears as a region of low light intensity adjacent to a region of high light intensity and the vortex centre lies along the common boundary between the two regions. The rapid change in light intensity is a direct result of the change in sign of the density gradient at the centre of the vortex. This fact enabled a rewarding series of experiments to be carried out on the behaviour of the wake using a standard schlieren system as the only instrumentation.

The cone-cylinder models had included nose angles of 15° and 20°. Both 0·4 and 0·5 in. diameter bodies were tested, and, depending on the model under test, a body length of 29 or 23 diameters was visible at any incidence. Typical results of these experiments are shown in figures 2–5 (plates 1–3). To assist in the interpretation of these photographs, further schlieren studies were carried out on a circular cylinder at a Reynolds number of approximately 10^5 and at Mach numbers up to 0·7. The cylinder was 1·10 in. in diameter and 13·5 in. long and was supported normal to the free stream by a slender central strut in the middle of the 15 in. square tunnel working section. Three-dimensional effects were therefore present (Humphreys 1960) but it is believed that these were not large enough to mask the predominantly two-dimensional wake. Schlieren photographs for $M = 0{\cdot}55$ and $M = 0{\cdot}70$ in figure 6 (plate 3) are therefore presented as being representative of two-dimensional wake flow patterns.

3.2. *Strouhal number of an unyawed circular cylinder at subsonic speeds*

The Strouhal number was determined by using a piezo-electric transducer to monitor the pressure fluctuations at a point near the upstream stagnation region on a 0·9 in. diameter cylinder mounted normal to the flow. Since the frequency of the pressure fluctuations is identical to the frequency of vortex shedding in the wake the Strouhal number can readily be obtained. Numerous test runs were made at Mach numbers between 0·3 and 0·65 for Reynolds numbers between $4{\cdot}3 \times 10^4$ and $2{\cdot}3 \times 10^5$. The Strouhal number was determined from the average frequency occurring at each flow condition and for all tests had a value of 0·21 to within a demonstrated uncertainty of 5 %. These results agree closely with those of Naumann *et al.* (1966) who have reported a Strouhal number of about 0·18 at low speeds increasing to 0·21 at $M_c = 0{\cdot}5$. Measured values of the Strouhal number are plotted in figure 15.

3.3. *Investigations of wake unsteadiness of inclined cone-cylinders*

The mercury arc continuous light source used in the schlieren system flickered noticeably and made observations on flow unsteadiness rather difficult to interpret. In certain incidence ranges a gross instability could be discerned very easily (see § 4.1) but for other incidence it was not certain whether changes seen on the viewing screen were due to small-scale unsteadiness or to the flickering light source. This was resolved by comparisons between photographs with different exposure times and a ciné film of the wake taken at 120 frames/sec. The regions of gross flow instability were photographed at 1300 frames/sec in an attempt to understand the instability mechanism.

For the Pitot and yawmeter pressure measurements (§ 3.4) the cone-cylinder model was mounted from a tunnel side wall and the steadiness of the wake could not be checked by direct observation. In order to remove any doubts on the flow behaviour a preliminary experiment was carried out in which a Pitot tube connected to a piezo-electric pressure transducer was traversed across the wake for one of the selected flow conditions. This showed conclusively that the flow pattern was steady.

3.4. *Wake traverses*

Six experiments were conducted in order to obtain an understanding of the flow within the wake at compressible speeds. In addition, an experiment was conducted at 100 ft/sec by Griss (1967) to provide wake data at incompressible speeds.

Some earlier wake traverses (Joregensen & Perkins 1958, for example) were conducted by attaching the measuring probe to the body and rotating the whole model in small angular steps in order to traverse the desired area of the wake.

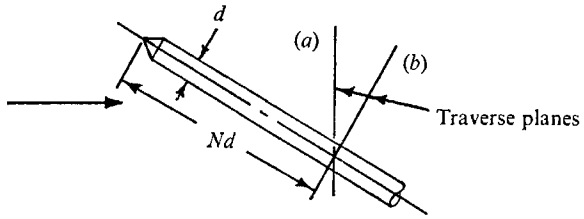

FIGURE 7

Test	M_0	R_c	Body diameter (in.)	Conical nose total angle (deg)	Traverse plane details
1	1·6	$5{\cdot}0 \times 10^4$	0·75	20	Type (*a*) N = 7·0, 8·5, 10·0, 11·5, 13·1, 13·8, 14·6, 16·1, 17·7, 19·2
2	1·6	$4{\cdot}4 \times 10^4$	0·75	20	Type (*b*) N = 16
3	1·6	$2{\cdot}8 \times 10^4$	0·6	20	Type (*a*) N = 25
4	2·0	$7{\cdot}5 \times 10^4$	0·75	15	Type (*a*) N = 18·5
5	2·4	$7{\cdot}5 \times 10^4$	0·75	15	Type (*a*) N = 18·5
6	2·4	$3{\cdot}8 \times 10^4$	0·6	20	Type (*a*) N = 25
7	V = 100 ft/sec	$5{\cdot}3 \times 10^4$	2·0	3 caliber ogive	Type (*a*) N = 23·2

TABLE 1. Details of wake traverse experiments, $\alpha = 30°$

However, Thomson & Morrison (1965) showed that rotation of the body could have a gross interaction on the wake. Thus, considering the flow in a cross-flow plane as being part of a vortex street, the hand of the vortices can be either left, right, left, ..., or right, left, right, ... depending on the misalignments at the nose of the body. It was found by the authors (1965) that a rotation of the body† about its axis could change the pattern from one vortex sequence to the other. In view of this the present tests were conducted with a fixed non-rotating body and the probe was attached to a separate traversing mechanism. The test conditions for the experiments are summarized in table 1 with (*a*), (*b*), *d*, *N* as shown in figure 7.

† This body was a cone-cylinder with a measured nose misalignment less than 5×10^{-4} in.

A 0·070 in. outside diameter Pitot tube was used in test 1 for wake traverses in ten planes normal to the free-stream direction. At the end of the traversing mechanism there was a canted fixture on which the Pitot tube was mounted at an angle of 15° to the tunnel centre-line in the plane containing the free-stream direction and the model centre-line. The axis of the Pitot tube was thus roughly

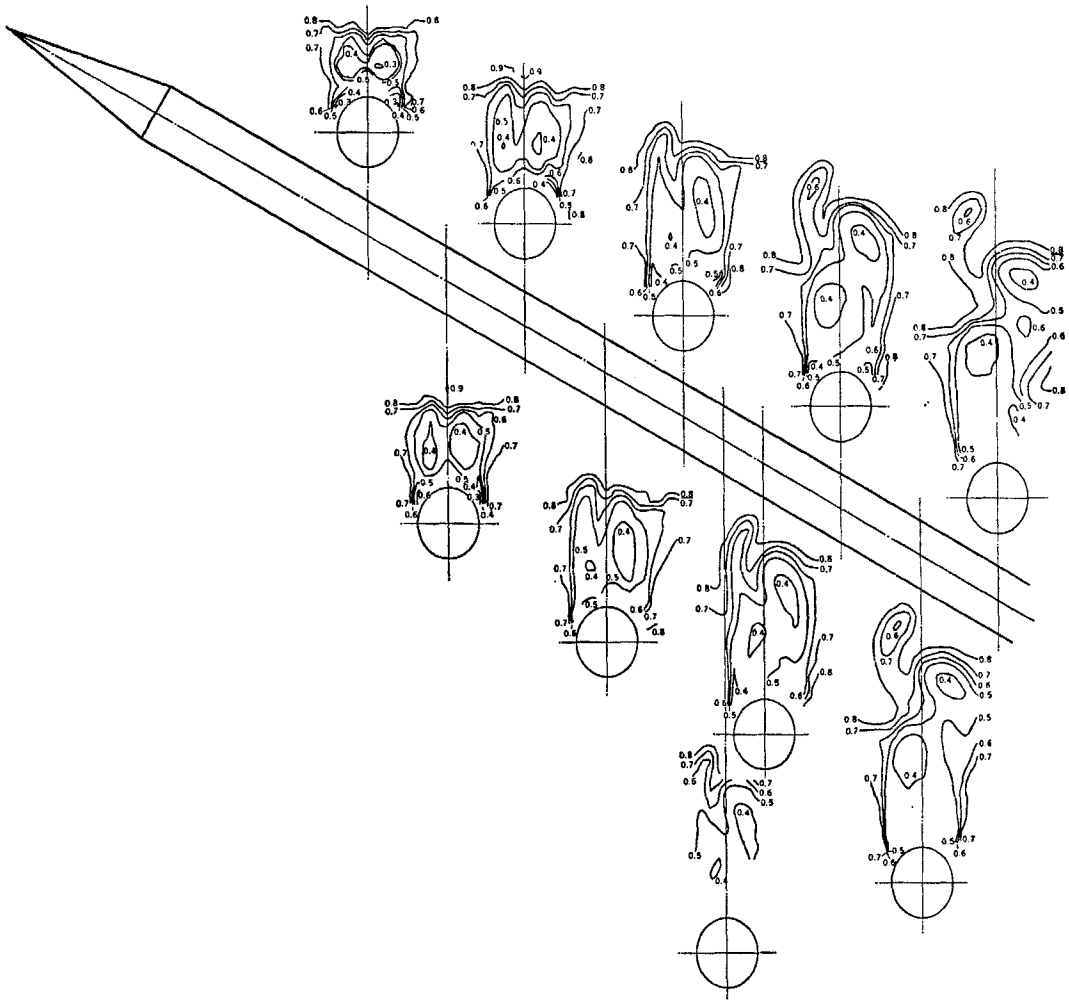

FIGURE 8. Test 1. Distribution of total head in the wake of a cone-cylinder at 30° incidence, contours of H/H_0. $M = 1{\cdot}6$, $R_c = 5{\cdot}0 \times 10^4$, total nose angle = 20°.

parallel to the shed vortices. This in general minimized the angle between the local flow direction and the probe and kept errors in Pitot pressure to a minimum. Nevertheless, there were still errors remaining owing to flow inclination caused by the vortex induced motion; no corrections were made to the results to allow for these errors. The results of this experiment are shown in figure 8 in the form of contours of uncorrected total pressure, non-dimensionalized with respect to the tunnel total pressure.

For tests 2–6 inclusive the local flow conditions were determined by means of a blunted 40° conical headed yawmeter probe of maximum diameter 0·105 in. The yawmeter was calibrated at Mach numbers between 1·4, and 2·8 and these results were subsequently extended by extrapolation to cover the Mach number range 1·3 to 3·2. Estimated errors from the use of the yawmeter are 1 % in Mach number and 0·5 % in total head at $M = 1{\cdot}3$, increasing to 3 % at $M = 3{\cdot}2$.

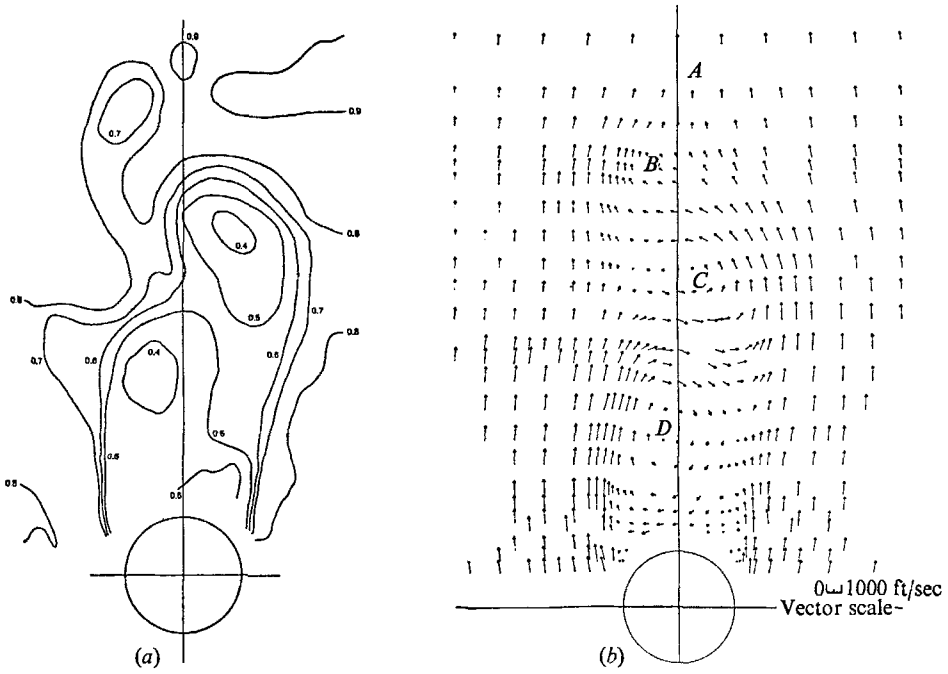

FIGURE 9. Test 2. Distribution of total head and velocity in cross-flow plane 16 diameters from nose. $\alpha = 30°$, $M = 1{\cdot}6$, $R_c = 4{\cdot}4 \times 10^4$, total nose angle = 20°. (*a*) Contours of H/H_0. (*b*) Vector velocity plot in plane normal to body, vortices *B*, *C*, *D* having $\Gamma/Vd \sin\alpha = 1{\cdot}25, -3{\cdot}20, 3{\cdot}30$ respectively (no value for *A*).

For each of the tests the yawmeter was mounted at 15° to the tunnel centre-line so that the probe axis was roughly parallel to the vortex paths. About 500 yawmeter readings were taken as each plane was traversed.

Figures 9–13 show results of these experiments. The results for test 2 are shown as distributions of total head and the velocity component in the traverse plane, while results from tests 3–6 show contours of total pressure, vorticity and local Mach number. The vorticity at each point was determined by finding the circulation about a square of side 0·1 in. surrounding that point and dividing by the area of the square. The overall error in vorticity is estimated to be $\pm 10^3\,\text{sec}^{-1}$; some idea of the significance of this error can be deduced from the fact that the general level of vorticity at the vortex centres is $\pm 10 \times 10^3$ to $\pm 80 \times 10^3\,\text{sec}^{-1}$.

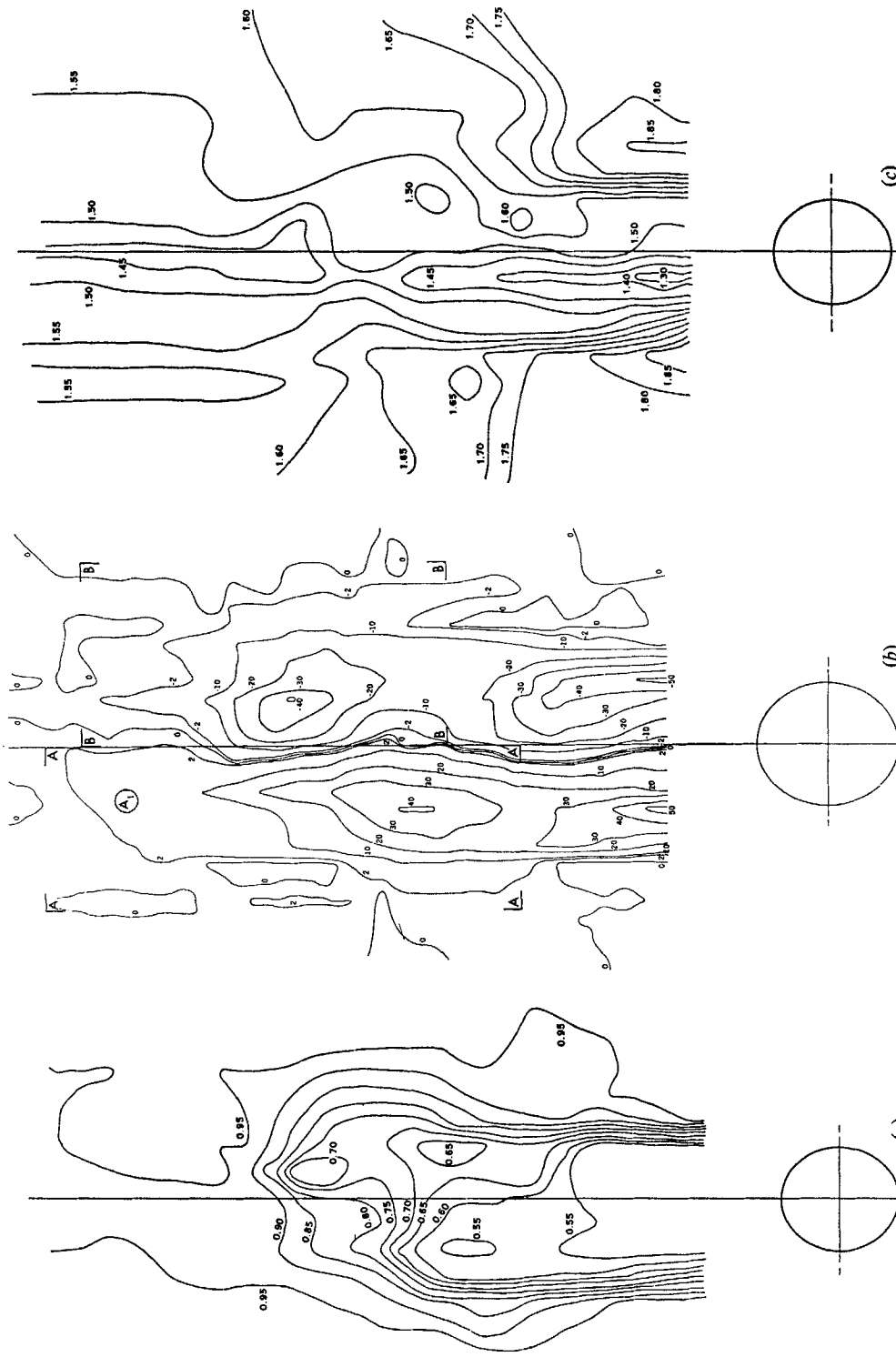

FIGURE 10. Test 3. Distribution of total head (*a*), vorticity (*b*) and local Mach number (*c*) in transverse plane 25 diameters from nose. $\alpha = 30°$, $M = 1{\cdot}6$, $R_c = 2{\cdot}8 \times 10^4$, total nose angle = 20°. (*b*) Shows contours of (vorticity/1000) sec^{-1}, $\Gamma/Vd \sin\alpha = 3{\cdot}98, -2{\cdot}88$ for areas *A*, *B* respectively.

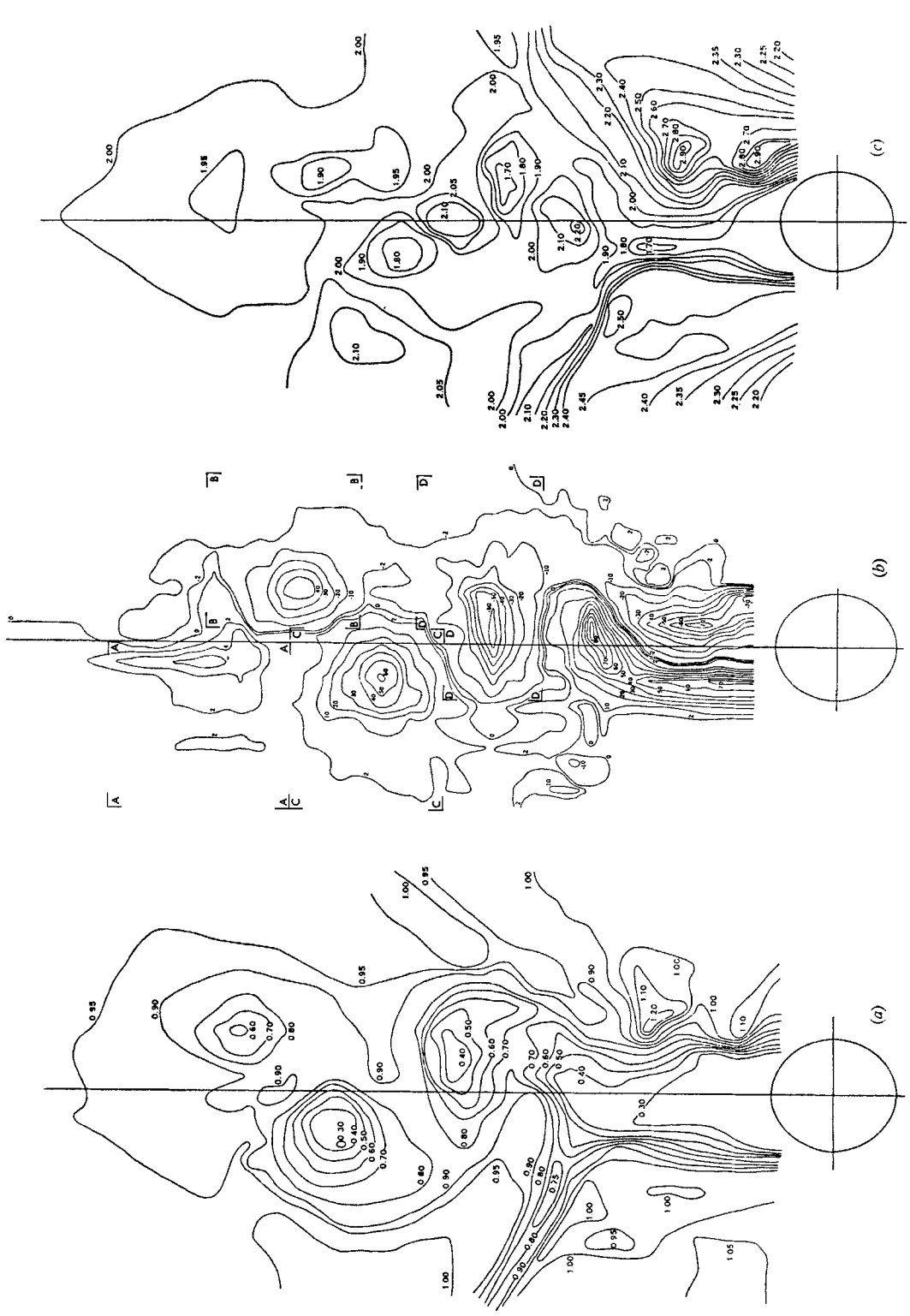

FIGURE 11. Test 4. Distribution of total head (*a*), vorticity (*b*) and local Mach number (*c*) in transverse plane 18·5 diameters from nose. $\alpha = 30°$, $M = 2{\cdot}0$, $R_c = 7{\cdot}5 \times 10^4$, total nose angle = 15°. (*b*) Shows contours of (vorticity/1000) sec^{-1}, $\Gamma/Vd \sin\alpha = 0{\cdot}36, -1{\cdot}11, 2{\cdot}05, -2{\cdot}03$ for areas *A*, *B*, *C*, *D* respectively.

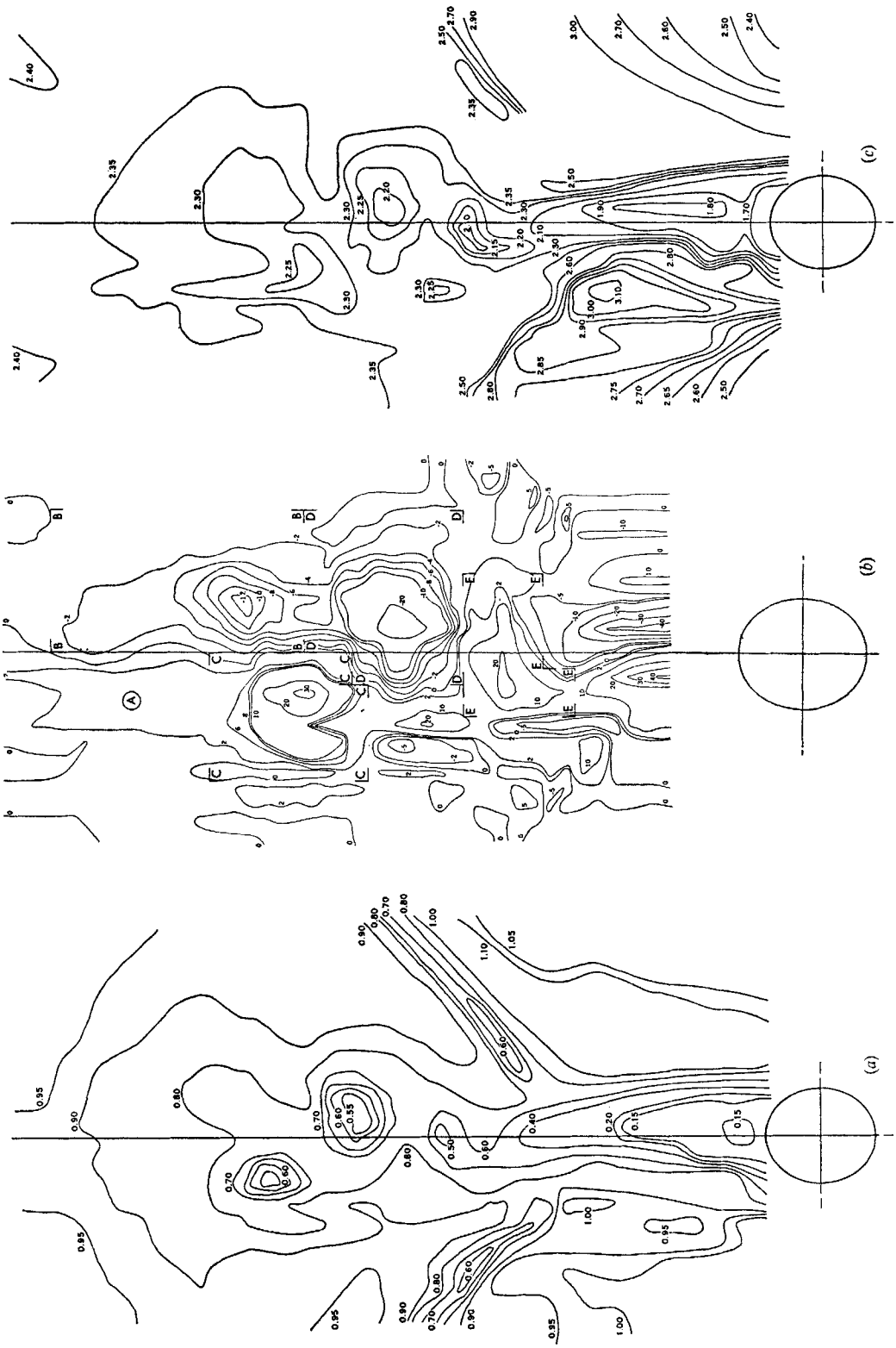

FIGURE 12. Test 5. Distribution of total head (*a*), vorticity (*b*) and local Mach number (*c*) in transverse plane 18·5 diameters from nose. $\alpha = 30°$, $M = 2{\cdot}4$, $R_c = 7{\cdot}5 \times 10^4$, total nose angle = 15°. (*b*) Shows contours of (vorticity/1000) sec^{-1}, $\Gamma/Vd \sin\alpha = -0{\cdot}50, 0{\cdot}75, -0{\cdot}75, 0{\cdot}50$ for areas *B*, *C*, *D*, *E* respectively (no value for *A*).

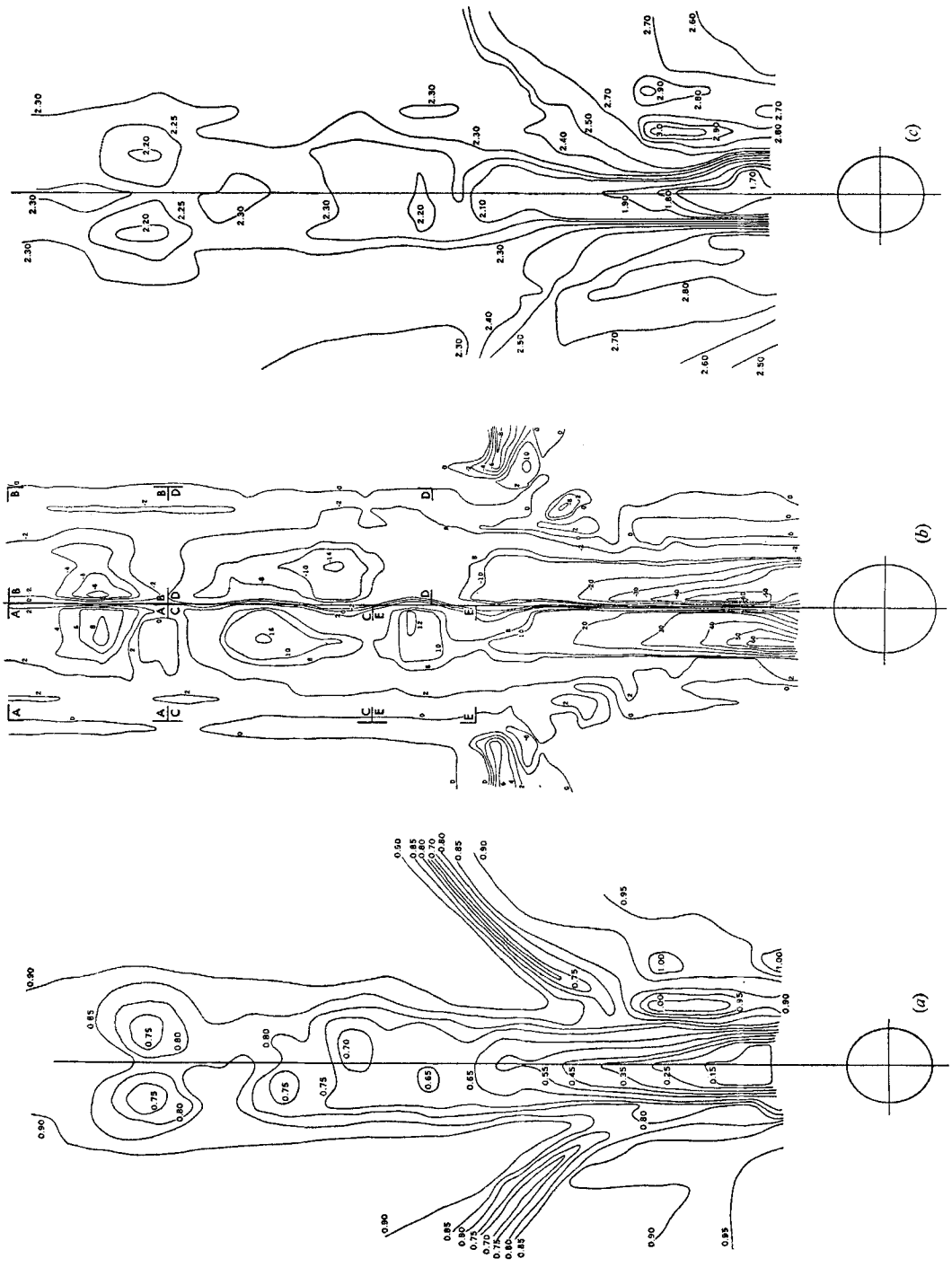

FIGURE 13. Test 6. Distribution of total head (*a*), vorticity (*b*) and local Mach number (*c*) in transverse plane 25 diameters from nose. $\alpha = 30°$, $M = 2{\cdot}4$, $R_c = 3{\cdot}8 \times 10^4$, total nose angle = 20°. (*b*) Shows contours of (vorticity/1000) sec^{-1}, $\Gamma/Vd \sin\alpha = 0{\cdot}29, -0{\cdot}27, 0{\cdot}75, -1{\cdot}03, 0{\cdot}46$ for areas *A*, *B*, *C*, *D*, *E* respectively.

4. Analysis of schlieren photographs

4.1. *General wake behaviour*

Two significant flow changes can be discerned in the wake pattern as Mach number, incidence and roll angle are changed. These can be conveniently described as a Mach number effect and a flow instability.

(i) *Mach number effect.* The Mach number effect is illustrated in figures 2 and 6. In the following discussion the cross-flow Mach number M_c will be used to link the flow patterns in figures 2 and 6. No compressibility effects can be discerned in the wake until M_c exceeds about 0·6, when shock waves appear between the rear of the body and the vortex street (figures 2(*b*) and 6(*b*)). In the two-dimensional flow pattern these shock waves are unsteady and the three-dimensional equivalent of this is a series of curved shock waves on the lee side of the cone-cylinder forming one behind the other in the lengthwise direction. The shock waves occur on either side of the central wake (see, for example, figures 6(*b*), 11(*a*), 12(*a*) and 13(*a*)) and when shown in silhouette in the schlieren photographs in figure 2 give the misleading appearance of overlapping. The shock waves can be detected just behind the cone-cylinder when $M_c = 0{\cdot}7$ (figure 2(*b*)) and further away from the body for M_c values of 0·8 and 1·0† (figures 2(*c*) and (*d*)). These flow patterns are cyclic, with respect to time in the two-dimensional case and with respect to distance along the body in the three-dimensional case.

For higher values of M_c the character of the wake changes (figures 2(*e*) and (*f*)). The shed vortices crowd together towards the nose and a triangular shaped area apparently free from discrete vortex cores develops between the body and the vortex street. The wave traverses (figures 12 and 13) show that intense shear layers exist in this region. The nose shock wave pattern ahead of the body also changes, moving progressively closer to the body and tending to become parallel to it as M_c is increased.

It is of some interest to link the photographs of figure 2 with the impulse flow analogy. When a two-dimensional cylinder is started impulsively from rest in a compressible fluid, first of all a starting shock wave moves out into the stream. If the speed of the cylinder relative to the stream is subsonic the starting shock will move out ahead of it, whereas if the relative speed is supersonic the shock wave will move to the appropriate stand-off distance and remain there. After the passage of the starting shock the wake pattern will develop on the downstream side of the cylinder and will rapidly approach its asymptotic state of either a cyclic variation with time or a predominantly steady flow pattern. Remembering that the flow photographs in figure 2 can be considered qualitatively as space–time plots of the above events, it is evident that the asymptotic wake pattern has been established in figures 2(*a*) to (*c*) but not in figures 2(*d*) to (*f*). In the latter figures, as already mentioned, the vortices tend to concentrate near the nose and a triangular shaped vortex-free area becomes apparent on the lee side of the body and grows with distance from the nose. There is no noticeable trend

† The shock waves appear as clear but very fine lines at $M_c = 1{\cdot}0$ and would not reproduce clearly in the printing process. Figure 2(*d*) has therefore been 'touched up' to make the shock waves more noticeable.

based on figure 2 for the boundary of this area to become parallel to the body. It is also evident that the starting shock does not reach its asymptotic configuration for any supersonic cross-flow Mach number up to 1·4 (figures 2(*d*) to (*f*)). However, it is likely that the starting shock would become parallel to a longer body. This change in flow pattern in the wake near $M_c = 1{\cdot}0$ may be expected to show in any detailed measurements made of schlieren photographs.

It will be shown later that significant changes in cross-flow Strouhal number and in the strength of the vortices occur for M_c near 0·7 and it is believed that the behaviour described above may be responsible for this.

(ii) *Flow instability.* For angles of incidence less than 30° the wake pattern is generally stable, but when the model is traversed through the range 30–40° a new phenomenon is observed. The wake pattern becomes unstable in certain incidence ranges which can extend from a fraction of a degree to several degrees. The stable wake patterns which exist before and after an unstable region always appear similar in schlieren photographs but the position of the vortex trails in relation to the body apex can sometimes change. This effect is shown in figure 3 at a free-stream Mach number of 0·8. Figure 3(*a*) shows the wake in its basic position. After the first region of instability it moves away from the nose to the position shown in figure 3(*b*). A further downward movement at a higher angle of incidence is shown in figure 3(*c*). The stable configurations shown in figures 3(*d*) and 3(*e*) each follow a region of instability as the wake moves back to its basic position. A puzzling feature of the wake patterns in figure 3 is the fine line which originates from the body apex and which has the characteristics of a weak vortex line.

Each of the photographs in figures 4 and 5 is separated by a region of instability. The wake patterns in figure 4 were obtained at a free-stream Mach number of 1·4 and show a movement downward and back up again, following the same general trend as in figure 3. Figure 5, which is a group of schlieren photographs at $M = 2{\cdot}8$, shows a marked decrease in the spacing between the vortices, indicating an increase in cross-flow Strouhal number, and also a gradual disappearance of the distinctive vortex paths downstream from the nose as incidence is increased. A further interesting feature of the flow pattern is the multitude of vortices which appear to be shed from the nose in place of the pair normally seen at lower Mach numbers. The vortices crowd together near the nose point and become further apart as the diameter increases, indicating possibly a link between vortex spacing and local diameter. This observation is reinforced by Gaster's (1969) low-speed experiments on very slender cones at 90° incidence in which he found that the frequency of vortex shedding is controlled by the local diameter.

In an attempt to define features of the flow in regions of instability a ciné film of the wake was made at free-stream Mach numbers of 1·4, 2·0 and 2·6, but even though the filming rate was 1300 frames/sec the wake fluctuations could not be resolved. Random flash photographs taken of one unstable situation showed the vortex system oscillating between the two stable configurations which existed on each side of the instability. In a further experiment a different cone-cylinder model with the same nose angle but presumably a different nose misalignment was set at 30° incidence and rolled slowly through 360°. Again, regions of wake

instability were detected, sometimes over a few degrees roll angle and in some cases extending over a range of about 20°. A final experiment was conducted in which for several preset angles of roll the incidence range was scanned and again unstable regions were observed.

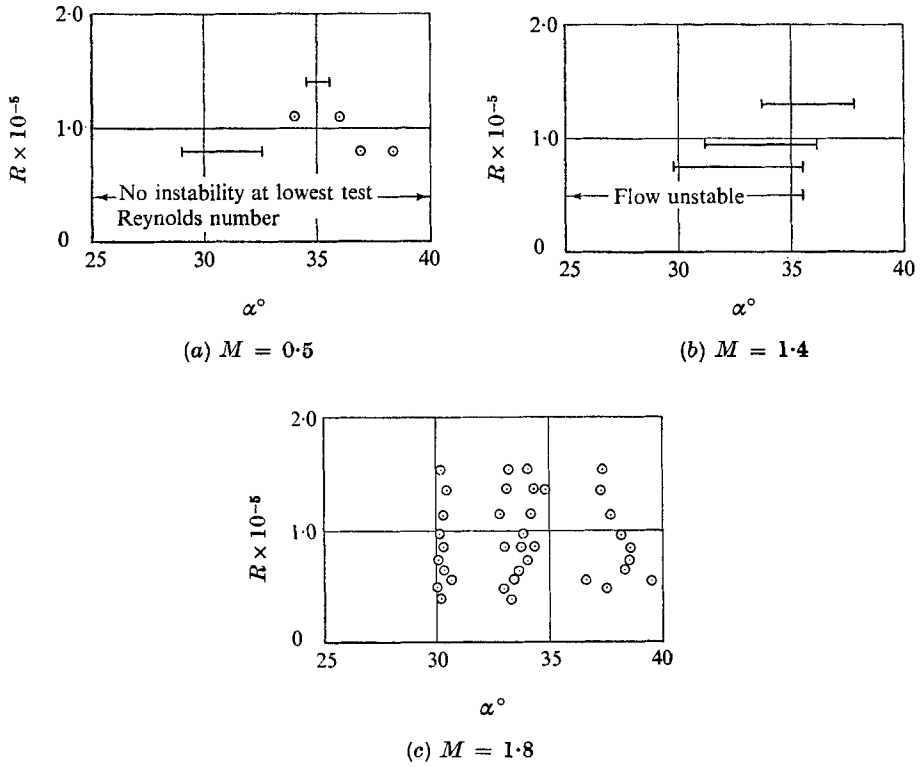

FIGURE 14. Regions of wake instability.

It is believed that the instability is somehow initiated by asymmetric flow very close to the nose, the asymmetry being due either to the orientation of the nose misalignment or to local flow direction changes caused by working section nozzle defects, or a combination of both.

Typical results for the particular tests in which the incidence was changed and roll angle kept constant are given in figure 14. At each free-stream Mach number the regions or points of instability were catalogued as incidence was varied at different values of free-stream Reynolds number based on the body diameter. The horizontal bars represent regions of continuous instability and the points represent localized unstable regions. These results seem to indicate that the Reynolds number has a strong effect on the region of instability. However, it may be that the Reynolds number has a small effect on free-stream flow misalignments but that these, through their influence at the model nose, have a large effect on wake stability.

4.2. *Strouhal number*

The values of Strouhal number have been obtained by measuring values of (g'/d) from photographs and inserting these into (1) which is based on the impulse flow analogy. All the results are plotted against cross-flow Mach number in figure 15. The points are marked with the relevant free-stream Mach number and show that this parameter is not significant. The Reynolds number is also not a significant parameter in the narrow range covered by the present tests.

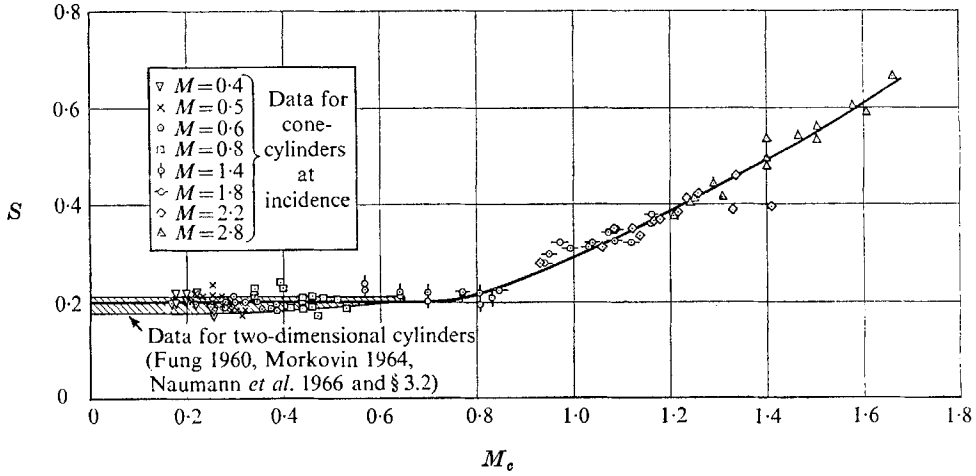

FIGURE 15. Cross-flow Strouhal number variation with cross-flow Mach number.

All the results collapse into a narrow band and can be represented quite well by a single line. Compressibility effects do not appear until $M_c \approx 0{\cdot}7$ which is well above the critical Mach number for a circular cylinder (about 0·4). As mentioned in § 4.1, this value of M_c corresponds approximately to the establishment of shock waves in the lee of the body.

A comparison of these results with the Strouhal number for a two-dimensional unyawed circular cylinder is also made in figure 15 using data presented by Fung (1960) and Morkovin (1964) for low speeds, Naumann *et al.* (1966) for $M_c \leqslant 0{\cdot}5$ and § 3.2 for $0{\cdot}3 \leqslant M_c \leqslant 0{\cdot}65$. The agreement between the two sets of data is striking and provides strong evidence supporting the impulse flow analogy in so far as Strouhal number, and therefore vortex spacing, is concerned.

4.3. *Position of vortex breakaway points*

As mentioned earlier, the nose misalignment determines whether the vortices are shed as a series handed left, right, left . . ., or right, left, right, ... A rotation of the body through a few degrees in roll or a change in incidence can cause the vortices to adjust from one system to the other and in doing so the positions where the vortices break away from the body vary. As well as individual vortices breaking away from different sides of the body the whole sequence of vortices can move as a unit slightly towards the nose or away from it. Hence an analysis of the

breakaway points from the body is expected to provide data containing an appreciable amount of scatter.

The schlieren photographs show that the vortex lines are straight except for a curved region near the body. A simplified picture of the wake can be obtained by considering the vortex lines to be straight throughout, in which case the vortex positions can be determined by locating the points C, D, E, F, etc. in figure 1 and by finding the angle ξ. The latter is examined in § 4.4 and in this section the determination of the distance g (figure 1) is considered.

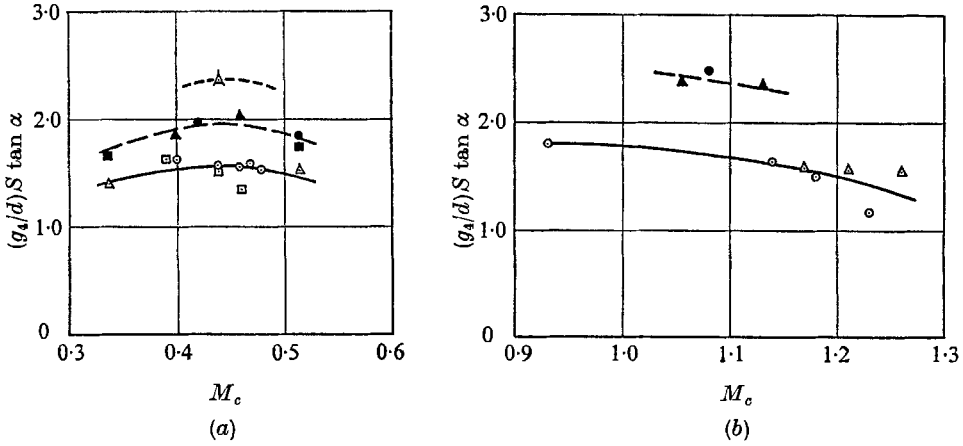

FIGURE 16. Possible effective starting positions of the fourth vortex. Total nose angle = 15°. ——, base wake configuration; – –, second configuration; · · · · ·, third configuration. (*a*) $M = 0{\cdot}8$; ⊙, $R = 1{\cdot}25 \times 10^5$; △, $R = 0{\cdot}71 \times 10^5$; ⊡, $R = 0{\cdot}40 \times 10^5$. (*b*) $M = 2{\cdot}2$; ⊙, $R = 1{\cdot}48 \times 10^5$; △, $R = 0{\cdot}77 \times 10^5$.

It is convenient to examine first the behaviour of what is judged to be the fourth vortex in the schlieren photographs. The wake traverses have revealed that the first vortex is very weak (§ 5) and the schlieren system is not sensitive enough for it to be detected in many cases. Hence the fourth vortex usually appears as the third one from the nose in the schlieren photographs.

The analysis is based on a parametric representation suggested by a re-arrangement of (1), namely

$$(g'/d)S\tan\alpha = 0{\cdot}5 = \text{constant}.$$

The distance g_4 (figure 1) is expressed in the non-dimensional form $(g_4/d)S\tan\alpha$ and typical results for two Mach numbers are plotted against cross-flow Mach number in figure 16.

It has been noted in § 4.1 that after a region of flow instability the wake pattern may shift downstream from the body apex. This effect is shown very clearly in figure 16. The points group around lines indicating stable configurations with increasing distance from the body apex. If the triangular symbols are followed at the free-stream Mach number of 0·8 (figure 16(*a*)), the movement downstream in two discrete steps followed by a double movement upstream can be compared with the series of photographs in figure 3. The majority of points in figure 16

lie on the line closest to the body apex, representing the basic wake position. The difference between these stable values of $(g_4/d)\,S\tan\alpha$, which might be expected to be 0·5 as given by the equation above, varies from 0·35 to 0·65 as the cross-flow Mach number increases from 0·35 to 1·1.

Now that the photographs representing the basic wake configurations can be identified the analysis becomes straightforward. Results for the starting positions of the third vortex in its basic configuration are shown in figure 17 as a function

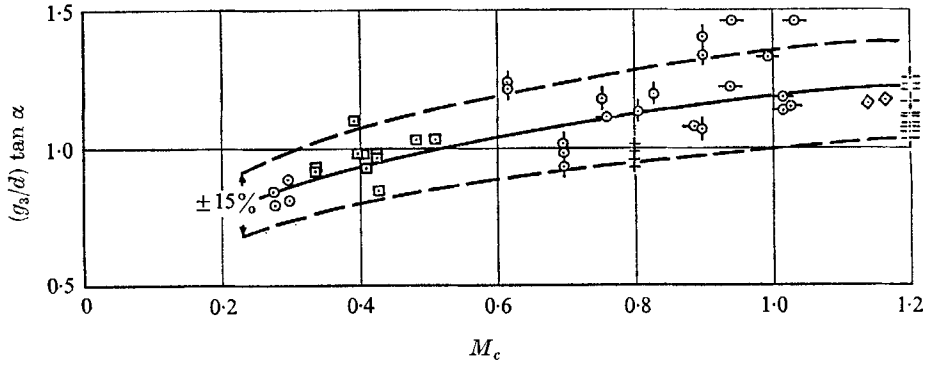

FIGURE 17. Starting positions of third vortex. Total nose angle = 15°. +, M = 1·6; ⊹, M = 2·4; other symbols refer to the same M values as in figure 15.

of M_c. These results are typical of the starting positions of all the vortices. The scatter of the points relating to the basic wake configuration is ± 1·3 body diameters for all cases and this rather large figure is a result of the experimental methods used. Part of the scatter could be due to the occurrence in some photographs of an observable first vortex which is mistakenly taken to be the second vortex. In these cases all vortices would be incorrectly labelled, which would result in spurious points being plotted on graphs such as figure 17. Points marked by crosses at M_c = 0·8 and M_c = 1·2 represent the range of $(g/d)\,S\tan\alpha$ values which occurred for the basic wake configuration when a particular cone-cylinder model was held at 30° incidence and rolled through 360°. There is thus some evidence that even the basic wake configuration is dependent on the nose misalignment. Figure 18 shows the lines of best fit for the complete wake pattern (basic configuration) plotted against cross-flow Mach number. These results apply for a cone-cylinder with a 15° total angle conical nose and do not necessarily hold for different cone angles. However, the distances of the fourth, fifth, sixth, ... vortices behind the third vortex are expected to be largely independent of the nose angle.

It should be noted that no systematic change in Strouhal number was observed for the second or third stable wake positions compared with that for the basic wake pattern.

4.4. *Angle between vortex lines and body centre-line*

ξ, the angle between the vortex lines and the body centre-line, has been presented in the form $\chi = \tan\xi/\tan\alpha$. χ has been determined from all the schlieren photo-

graphs and is shown plotted against M_c in figure 19, together with the best fit line through the points. There is considerable scatter, equivalent to a maximum error in ξ of approximately $\pm 2{\cdot}5°$, which, it is believed, is due to difficulties in interpreting schlieren photographs, particularly at low values of M_c. Many of

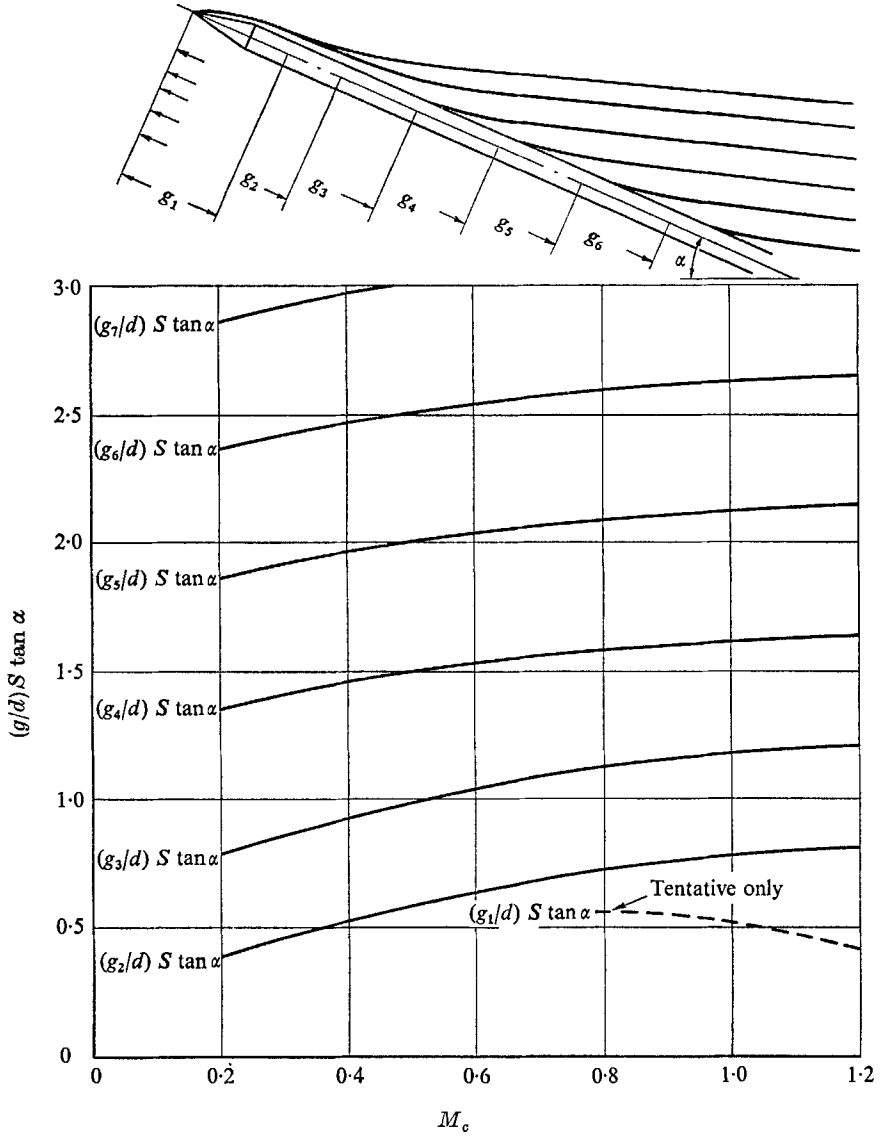

FIGURE 18. Starting positions of all the vortices in the wake. Total nose angle = 15°.

these points were obtained by analysing photographs taken at low angles of incidence when the straight parts of the vortex lines occurred well downstream from the nose and just in the field of view. Other points were taken from high incidence photographs, but the density gradients near the vortex centres in the flows at the lower speeds were so small that the schlieren pictures were indistinct.

Under these circumstances errors in measuring ξ were sufficiently large to cause the scatter shown in figure 19.

A distinct minimum occurs in χ at $M_c \approx 0{\cdot}7$ which is close to the value of M_c at which the cross-flow Strouhal number shows a change in behaviour (figure 15).

4.5. *Lateral spacing and strength of vortices in wake of inclined cone-cylinders*

The impulse flow analogy provides a convenient way of describing the flow development past a slender body at incidence, but so far there has been no adequate quantitative check on its validity. Thomson & Morrison (1969) used equation (5) together with the vortex spacing ratio deduced by Kármán for vortex

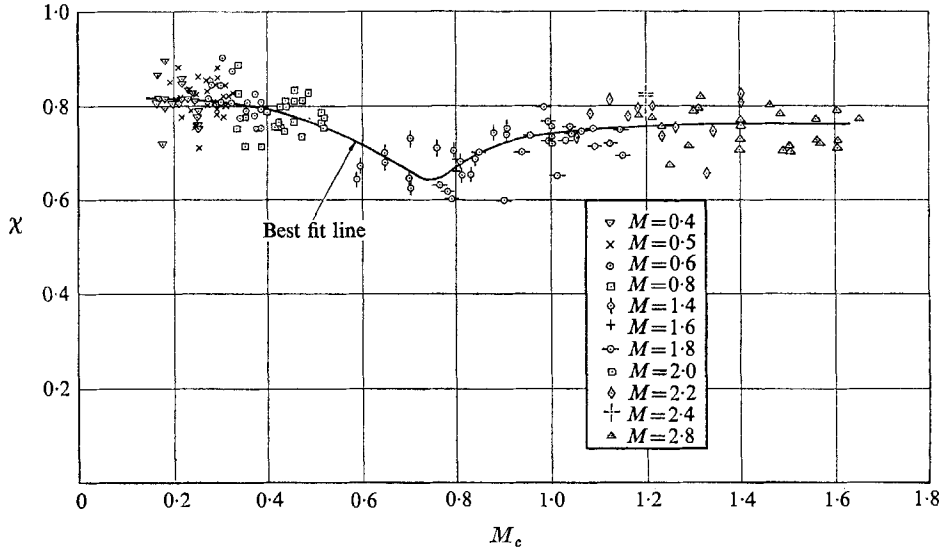

FIGURE 19. Variation in wake parameter χ with cross-flow Mach number.

street stability (i.e. $h/l = 0{\cdot}281$) and obtained reasonably good correlation between the vortex strengths deduced from schlieren photographs and those from wake traverses. On this basis they concluded that the impulse flow analogy could be used quantitatively. However, the vortex spacing ratio used did not match that found from wake traverses; in addition, many workers (e.g. Wille 1966) have reported large deviations from the Kármán spacing ratio. It is therefore concluded that the good correlation achieved was not dependent on the spacing ratio and, by (5), the significant parameter must be $(l/d)(1-\chi)$, or $\chi(1-\chi)/S$.

In contrast with this, there is little doubt that the sweepback principle is applicable to the analysis of a yawed vortex street except in the vortex cores where, at the Reynolds numbers of interest here, three-dimensional velocity fluctuations will occur. (Following Schlichting's (1968) discussion on the viscous flow development on an infinite yawed wing, it is apparent that these velocity fluctuations will not allow decoupling of the normal and transverse equations of motion.) In the potential flow analysis in § 2 only the overall flow field is

examined and on this scale of observation turbulence in the vortex cores is not expected to affect the applicability of the sweepback principle.

Equation (9) is therefore preferred to (5) for estimating the vortex strength. In order to apply this equation it is necessary to determine h/l and for this purpose the results of the wake traverses given in § 5 are anticipated. Figure 20 shows

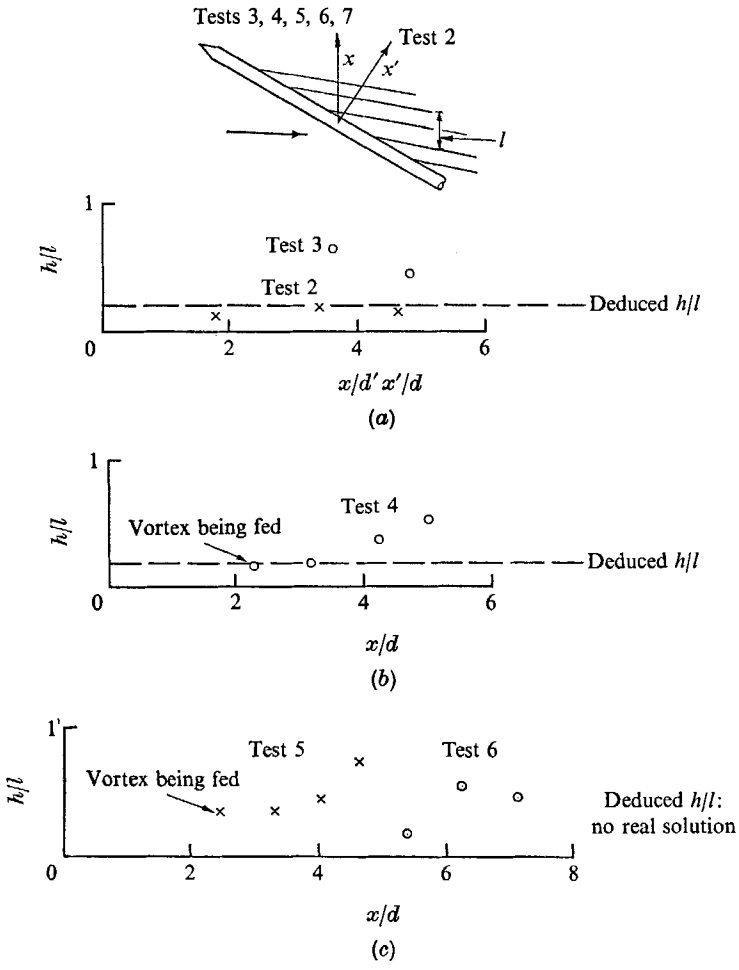

FIGURE 20. Vortex spacing ratio in wake of cone-cylinder at incidence. Test 7 gave deduced $h/l = 0{\cdot}18$.

values of h/l measured from the wake traverses in figures 9–13. Although there is considerable scatter in the results a definite trend occurs for the vortex streets to broaden as vortices move away from the body, in agreement with the results reported by Wille (1966) for a cylinder in two-dimensional incompressible flow. Unfortunately the widening vortex streets in figure 20 do not permit a logical choice to be made for h/l. Therefore vortex strengths obtained from the wake traverses in tests 2–7 have been substituted into (9) to determine values of h/l. This gave $h/l = 0{\cdot}20$ for tests 2 and 3, $0{\cdot}18$ for test 4, no real solution for tests 5

and 6, and 0·18 for test 7. These values define the spacing ratios of constant width Kármán vortex streets which have the same strength vortices and transport speeds as in the real broadening vortex streets. The results are shown plotted in figure 20. For tests 2 and 4 the deduced h/l values agree fairly closely with measured h/l values for vortices near the body. The curious result of no real solution for tests 5 and 6 will be discussed later. For the Reynolds numbers covered, h/l varied remarkable little for cross-flow Mach numbers up to 1·0 and for the present purposes it is adequate to use a constant value, $h/l = 0{\cdot}19$, in (9).

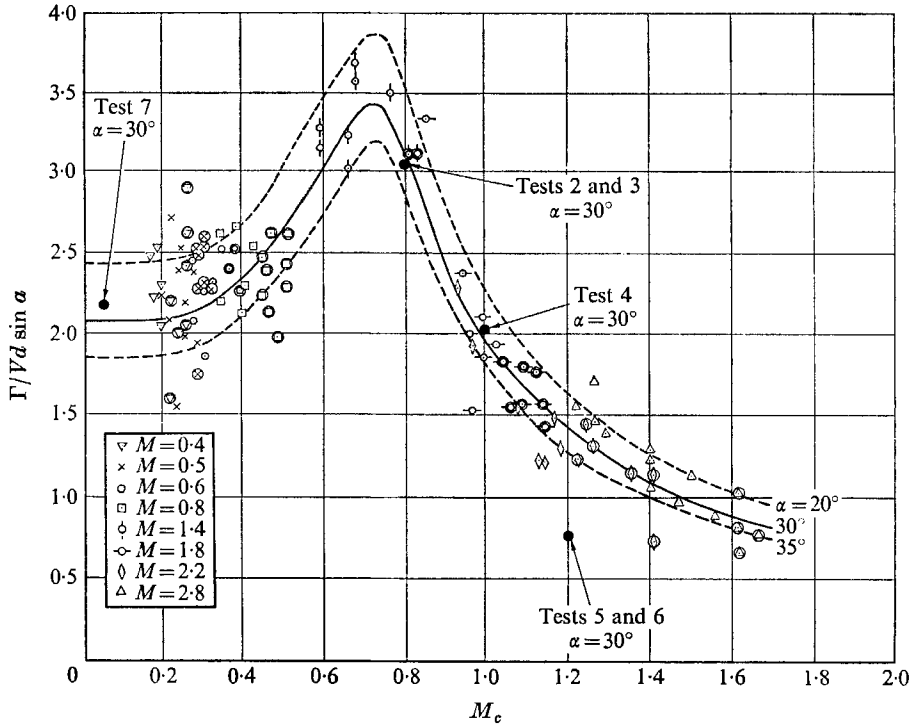

FIGURE 21. Vortex strength estimated from schlieren photographs and wake traverses. Incidence range: unfilled data points, $22° \leqslant \alpha \leqslant 35°$; encircled points, $\alpha \geqslant 30°$; filled data points, wake traverses, $\alpha = 30°$. M values were obtained from data from schlieren photographs, $h/l = 0{\cdot}19$, and using the sweepback principle; ——, – – –, deduced using mean χ and S at each M_c.

Individual values of χ and S have been substituted into (4) to find d/l, and then into (9) to give values of $\Gamma/Vd\sin\alpha$ which have been plotted in figure 21. In addition, the mean values of χ and S from figures 19 and 15 respectively have been used to produce the lines shown in figure 21 for body incidences of 20, 30 and 35°. The scatter of the points is due chiefly to the scatter in χ. The curves for $\alpha = 20°$ and $\alpha = 35°$ are seen to bracket most of the points which were obtained from schlieren photographs over the incidence range $22° \leqslant \alpha \leqslant 35°$. Points corresponding to $\alpha \geqslant 30°$ have been encircled and for $M_c > 0{\cdot}4$ a trend can be discerned for them to lie below the unmarked points, in general conformity with the disposition of the three curves in figure 21.

The distinct peak in the values of $\Gamma/Vd\sin\alpha$ arises from the minimum in χ at $M_c \approx 0{\cdot}7$. From the form of this curve it appears that the 'transonic range' of the wake is restricted to a small region near $M_c = 0{\cdot}7$; below this value the wake has subsonic characteristics while above it the supersonic type of characteristics are in evidence.

It is interesting that the use of vortex street theory combined with the sweepback principle leads to a collapse of data from schlieren photographs into a narrow band beyond $M_c = 1{\cdot}0$, even though the vortex spacing ratio was found for $M_c \leqslant 1{\cdot}0$, and deduced vortex strengths for higher values of M_c are apparently wrong. It is also remarkable that the basic character of the flow described by the Kármán vortex street theory is retained in the compressible flow régime, right up to $M_c = 1{\cdot}0$. As mentioned earlier the dominant features which define vortex strength appear to be described by the parameter $(l/d)(1-\chi)$ common to both (5) and (9). Beyond $M_c = 1{\cdot}0$ it is probable that the vortex street theory, rather than the sweepback principle, ceases to hold. Figures 2(*e*), 2(*f*), 12 and 13 show that a broad vortex street still exists, but the Kármán theory requires a progressively narrowing wake as M_c is increased beyond 1·0. The reason for no real solution for h/l in tests 5 and 6 (figure 20) is that the spacing ratio is required to decrease to the extent that it becomes negative. The change in flow pattern near $M_c = 1{\cdot}0$, described in §4.1(i), may be indicative of the wake changing from what might be termed the Kármán régime into another (undefined) régime. If the vortex strength derived from the application of the sweepback principle is accepted, then application of the impulse flow analogy will lead to an erroneous vortex strength, the magnitude of which is given by equation (10). As an example of the error, when $M_c \leqslant 0{\cdot}4$ the impulse flow analogy gives a vortex strength too large by 30 % at $\alpha = 30°$, increasing to 65 % at $\alpha = 40°$.

5. Analysis of wake traverses

5.1. *Test* 1

The total pressure distributions in figure 8 show the existence of a symmetric vortex pattern in the wake at the furthest forward traverse plane. Farther downstream the flow loses its symmetry but the mechanism by which the asymmetry develops is not clear. One vortex appears to elongate and then separate into two vortices, one of which detaches while the other still remains attached to the feeding sheet. Further downstream the vortex street development can be clearly seen.

5.2. *Tests* 2 *and* 3

Figures 9(*a*) and (*b*) enable four† vortices to be discerned in the wake at $M = 1{\cdot}6$ at a distance of 16 diameters from the nose. The circulations of the vortices marked *B*, *C* and *D* in figure 9(*b*) were found by integrating the cross-flow velocity

† The outermost vortex cannot be readily discerned from figure 9. However, if the local cross-flow wake transport velocity is subtracted, so that the observer is moving with the cross-flow rather than with the body, a very weak vortex can be detected in the region marked *A*. This technique was used to determine the centres of vortices *B*, *C* and *D*.

around rectangular contours containing each vortex core. The area of each rectangle was increased in a systematic manner until the contour integral ceased to increase, indicating that all the vorticity had been contained within the rectangles. For the vortex marked B the final area enclosed in the rectangle was 1·5 times the body cross-sectional area, while for vortices C and D areas 2·8 times the body cross-sectional area were required. It is surmised that considerable diffusion of vorticity had occurred. The vortex strengths given by this method are as follows:

Test 2

Vortex	A	B	C	D
$\Gamma/Vd\sin\alpha$	—	$+1{\cdot}25$	$-3{\cdot}20$	$+3{\cdot}30$

Vortices C and D are considered to be representative of those in the equivalent vortex street.

Further downstream in a plane 25 diameters from the nose (figure 10(*b*)) the vortices are not completely separated from each other. Each vortex core appears as a concentration of vorticity in an overall plateau. Thus the vortex marked B is joined by an area of vorticity to the concentration of vorticity nearer to the body. Similarly, the large elongated vortex marked A is joined by a shear layer to the flow in close proximity to the body. In order to try and treat these areas of vorticity as isolated vortices the rectangular boundaries marked A and B have been chosen by eye to give a reasonable demarcation of the extent of the vortices. Integrating over these areas leads to the following circulations:

Test 3

Vortex	A	B
$\Gamma/Vd\sin\alpha$	$+3{\cdot}98$	$-2{\cdot}88$

More vortices appear in the relevant schlieren photograph† than were detected in the wake of the model used in test 3. In view of the size of vortex A it is conjectured that one of the first two vortices shed and one of those representative of the vortex street may have joined together. Test 3 vortices could therefore possibly be represented as follows:

Vortex	A_1	A_2	B
$\Gamma/Vd\sin\alpha$	$+1{\cdot}10$	$+2{\cdot}88$	$-2{\cdot}88$

These results are in reasonable agreement with those for test 2, which provides support for the above conjecture.‡ On this basis the results of test 2 and the modified results of test 3 can be represented by the following mean values with a maximum deviation of 7 %. For the stronger of the first two vortices shed, $\Gamma/Vd\sin\alpha = \pm 1{\cdot}17$; for vortices representative of the vortex street,

$$\Gamma/Vd\sin\alpha = \pm 3{\cdot}06.$$

The fact that the vortices were stronger in test 2 than in test 3 may indicate a decay in circulation between stations 16 and 25 diameters from the nose.

† Not included, but this point is covered in § 5.6.

‡ Since the circulation of a vortex is independent of the path of integration and is a scalar quantity its value does not depend on the plane in which the traverse is made. Hence it does not matter that for test 2 the traverse plane was normal to the body and for test 3 it was normal to the free stream.

5.3. *Test* 4

Figure 11 shows the flow details in a plane 18·5 diameters from the nose at a Mach number of 2·0. The vortices are particularly distinct and form a pattern closely analogous to the classical vortex street. The curves of total head and Mach number distribution reveal the existence of shock waves between the body and the region where the vortex street starts. This feature is similar to that described by Hall *et al* (1959) for a symmetrical wake. Areas exist in figure 11 (*a*) between the shock waves and the body where the total head is apparently greater than the free-stream value. This effect is believed to be due to the fact that the measuring probe axis was nearly parallel to the shock waves; when positioned close to the body the probe would pierce the shock waves obliquely and extensive interference would be expected. Although the vortex centres can be found from the areas of low total head (figure 11 (*a*)) the Mach number contours (figure 11 (*c*)) are misleading with too many apparent centres being present.

The four vortices in figure 11 (*b*) were considered to lie within the areas marked *A*, *B*, *C* and *D*, and integration of the vorticity distribution gave the following values for circulation:

Test 4

Vortex	*A*	*B*	*C*	*D*
$\Gamma/Vd\sin\alpha$	+0·36	−1·11	+2·05	−2·03

The vortices marked *A* and *B* appear to be the first two vortices shed while *C* and *D* correspond to the first two vortices of the equivalent vortex street.

5.4. *Tests* 5 *and* 6

Shock waves in the wake can be clearly discerned in the results of both tests 5 and 6 (figures 12 and 13). In test 5 there is a blank area between the body and one shock wave where the yawmeter probe was in flow conditions outside the range of its calibration. As for test 4, the regions of low total head can be used to determine centres of vorticity but again the Mach number pattern is misleading. Although the centres of vorticity are reasonably well defined in figure 12 (*b*), they are embedded in an area of vorticity and the boundaries of the vortices cannot be defined with any certainty. As for other tests, boundaries were chosen by eye to give a reasonable demarcation of the extent of the vortices; this gave five areas of vorticity with the following vortex strengths:

Test 5

Vortex	*A*	*B*	*C*	*D*	*E*
$\Gamma/Vd\sin\alpha$	—	−0·50	+0·75	−0·76	+0·50

The region marked *A* is believed to indicate the first vortex which is very weak, *B* is the second vortex, while *C* and *D* are the first two vortices in the equivalent vortex street. The region *E* marks where the next vortex is growing. However, it has not yet separated from the body boundary layer and the inter-connecting shear layer can be clearly seen.

The results for test 6 (figure 13(*b*)) show that the contour of zero vorticity has changed from a sinuous to an almost straight line as the traverse plane is moved from 18·5 to 25 diameters from the nose. There is no longer a close resemblance to the classical vortex street and the vortex cores appear as relatively indistinct centres of vorticity embedded in a region of high shear. The areas of demarcation of vortices are more difficult to determine than for test 5. The weak vortices A and B seem to be reasonably separated from the rest of the wake and presumably represent the first two vortices shed. Vortex strengths based on the chosen boundaries shown in figure 13 are as follows:

Test 6

Vortex	A	B	C	D	E
$\Gamma/Vd\sin\alpha$	$+0{\cdot}29$	$-0{\cdot}27$	$+0{\cdot}75$	$-1{\cdot}03$	$+0{\cdot}46$

On the basis of the earlier experiments C, D and E could be considered vortices in the equivalent vortex street. The average strength is $\Gamma/Vd\sin\alpha = \pm 0{\cdot}75$ which agrees well with the results of test 5. The large scatter could be due in part to the difficulty in choosing boundaries of integration about each vortex core.

5.5. *Test 7*

The results of Griss (1967) were analysed in a manner similar to that used for test 2 and yielded $\Gamma/Vd\sin\alpha = 2{\cdot}18$. The cross-flow Reynolds number of this test was $R_c = 5{\cdot}3 \times 10^4$.

5.6. *Breakaway points of first vortex*

It was stated in § 4.3 that the first vortex could not usually be seen in schlieren photographs. The reason for this is that the first vortex is as a rule very weak, as indicated by the results of tests 2–6. These tests have also provided the approximate position of the first vortex in four of the five experiments (the outermost vortex for test 3 cannot be discerned). The results are shown plotted in figure 22 together with estimated positions of all the other vortices, using the data in figures 18 and 19. The broken lines in the figure are the estimated paths of the first vortex in the series of wake traverses and their intercepts with the body axis have been used to provide the tentative estimate of $(g_1/d)S\tan\alpha$ shown in figure 18.

The positions of the vortex centres for test 1 have been determined from figure 8 and superimposed on the top diagram in figure 22. It is seen that correlation is reasonably good provided the predicted position of the first vortex is ignored. The comments made in § 4 may be relevant in explaining this discrepancy, namely the effect of nose misalignment orientation and the difficulty in determining the path of the first vortex from schlieren photographs. This comparison shows that the simplified representation of the vortex paths is a poor approximation near the body.

In passing, it is pointed out that the predicted paths of the vortices lie closer to the vortex centres in tests 4 and 5 (15° nose angle) than for tests 2, 3 and 6 (20° nose angle). This is to be expected in view of the fact that the predictions

were based on schlieren photographs of a 15° nose angle cone-cylinder. The results for the 20° nose angle cone-cylinder show more scatter but on the basis of the data under review there is insufficient evidence to indicate a significant displacement of the vortex pattern due to small changes in nose angle.

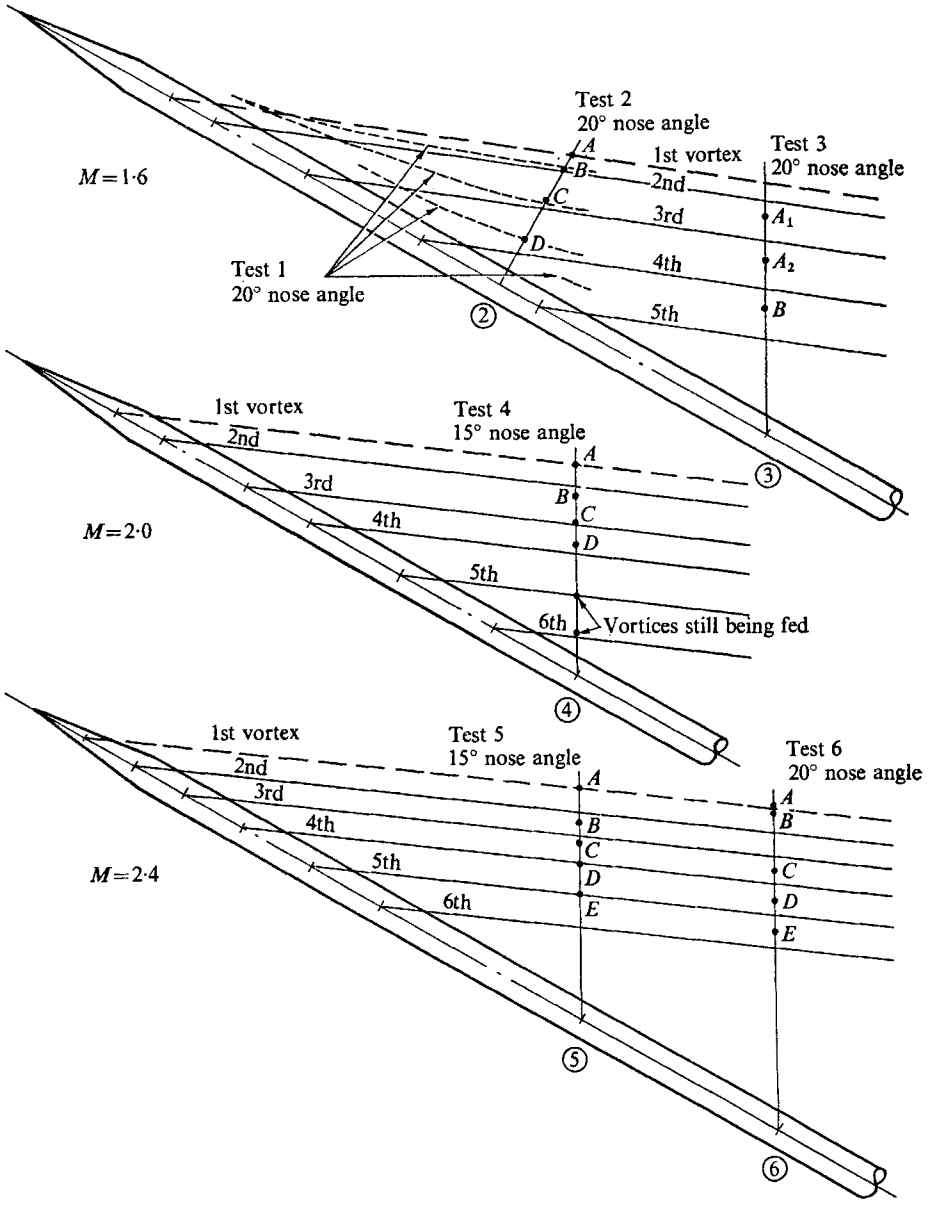

FIGURE 22. Comparison between measured and deduced vortex positions for tests 1 to 6. ——, deduced paths of vortices from cone-cylinder with 15° total angle nose, from figures 18 and 19; $\alpha = 30°$.

6. Vortex strength and vortex drag for a two-dimensional circular cylinder

It is of interest to determine the strength of the vortices in the wake of an unyawed two-dimensional circular cylinder and (6)–(9) enable this to be done. In this case, for which the wake is unsteady, the vortices are parallel to the cylinder axis and therefore $\xi = \chi = 0$. Equation (7) therefore becomes $l_s = l$, equation (8) becomes $U_s = V$, and equation (9) becomes

$$\Gamma/Vd = \Gamma/U_s d = 2(l_s/d)\coth(\pi h/l_s), \tag{11}$$

which can also be found directly from (6).

It is noted in (11) that Γ is expressed in terms of U_s, the speed of the wake behind the moving cylinder, and it would be preferable to express Γ in terms of the cylinder speed, which is defined as U_c.

Now

$$\frac{\Gamma}{U_c d} = \frac{\Gamma}{U_s d}\cdot\frac{U_s}{U_c}. \tag{12}$$

Also $S = nd/U$. But

$$n = U_c - U_s/l_s = (U_c/d)(1 - U_s/U_c)\, d/l_s$$

and therefore $\quad S = d/l_s(1 - U_s/U_c) \quad$ or $\quad U_s/U_c = 1 - S l_s/d.$

Hence from (11) and (12)

$$\Gamma/U_c d = 2l_s/d\,(1 - S l_s/d)\coth(\pi h/l_s). \tag{13}$$

It has been demonstrated in § 4.2 that application of the impulse flow analogy to slender cone-cylinders at incidence leads to Strouhal number measurements which are the same as those for an unyawed two-dimensional circular cylinder. It follows therefore that d/l given by equation (4) and evaluated using figures 15 and 19 will be the same as d/l_s in (13). For the purpose of determining $\Gamma/U_c d$ a constant value of $h/l_s = 0{\cdot}19$ has been chosen for the spacing ratio, in accordance with the discussion in § 4.5. The derived vortex strength is shown in figure 23 for Mach numbers up to 1·0. Also shown is a range of vortex strengths for incompressible flow and subcritical Reynolds numbers estimated† on the basis of Prandtl's formula for the strength of the shear layer from a circular cylinder. These two sets of data are seen to agree closely.

† According to Prandtl (see Birkhoff & Zarantonello 1957) the rate at which circulation in the shear layer on each side of a circular cylinder passes into the vortex street is given by $(1+Q)\,U_c^2/2$, where Q is minus the pressure coefficient in the region of flow separation. The feeding time from vortex formation to vortex detachment from the cylinder is $1/n$, and, by Prandtl, only about half the circulation in the shear layer appears in the vortices. (Both Fage & Johansen (1927) and Abernathy & Kronauer (1962) quote a figure of approximately 0·6.) Hence the strength of a vortex is given approximately by

$$\Gamma = (1+Q)\,U_c^2/4n,$$

or, in terms of Strouhal number,

$$\Gamma/U_c d = (1+Q)/4S.$$

For subcritical Reynolds numbers Q has values 1·0 to 1·2 (Goldstein 1950) and for $S = 0{\cdot}20$ this equation gives $\Gamma/U_c d = 2{\cdot}5$ to 2·75.

Finally, figure 23 enables Thomson's (1970) estimate of the vortex drag of a circular cylinder to be updated. The previous estimate was based on a vortex strength derived by application of the impulse flow analogy and the Kármán vortex spacing ratio, $h/l = 0{\cdot}281$. Kármán's expression (Durand 1935) for vortex drag coefficient is

$$C_D = (l_s/d)\,[1{\cdot}588\,U_s/U_c - 0{\cdot}628(U_s/U_c)^2],$$

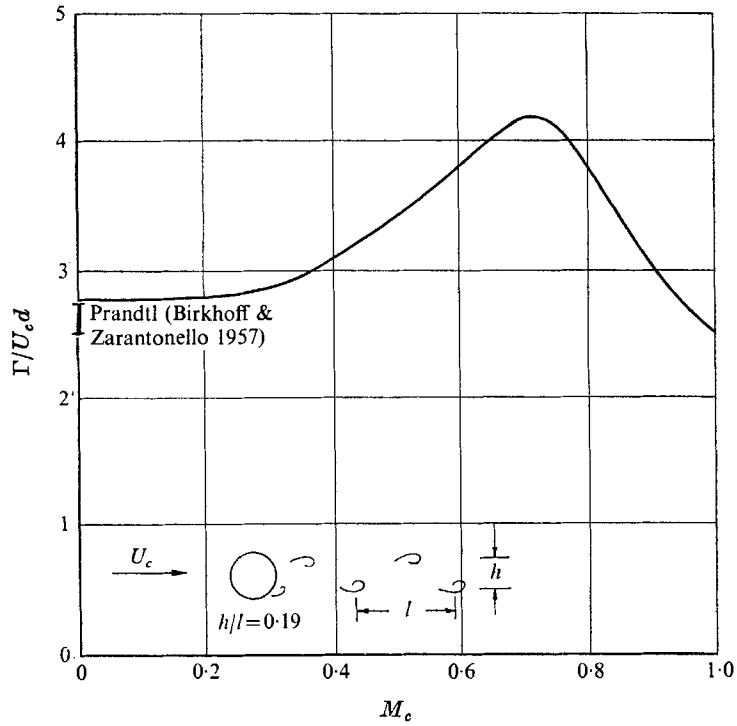

FIGURE 23. Deduced strength of wake vortices from two-dimensional circular cylinder at subcritical Reynolds numbers.

which, by use of (11), can be rewritten

$$C_D = 0{\cdot}794\left(\frac{\Gamma}{U_c d}\right)\tanh\left(\frac{\pi h}{l_s}\right) - 0{\cdot}157\left(\frac{d}{l_s}\right)\left(\frac{\Gamma}{U_c d}\right)^2\tanh^2\left(\frac{\pi h}{l_s}\right). \tag{14}$$

Substituting into (14) values of vortex strength from figure 23, and assuming $h/l_s = 0{\cdot}19$, leads to the estimated drag coefficient in figure 24, where close agreement with experiment is seen to exist up to Mach number of 0·8. The discrepancy at higher Mach numbers is believed to be due to a rapid increase in the wave drag not to a failure in the method, as explained in detail by Thomson (1970).

7. Conclusions

From the experiments it is concluded that in the cross-flow Reynolds number range $2{\cdot}7 \times 10^4$ to $7{\cdot}5 \times 10^4$ the wake development behind a slender cone-cylinder at large angles of attack is not exactly analogous to the development of the wake

from a circular cylinder started impulsively from rest. Analysis of the wake by means of the impulse flow analogy leads to a Strouhal number which is the same as that for a two-dimensional circular cylinder but the vortex strength is over-estimated. Neglecting the first two or three vortices which have been shed from

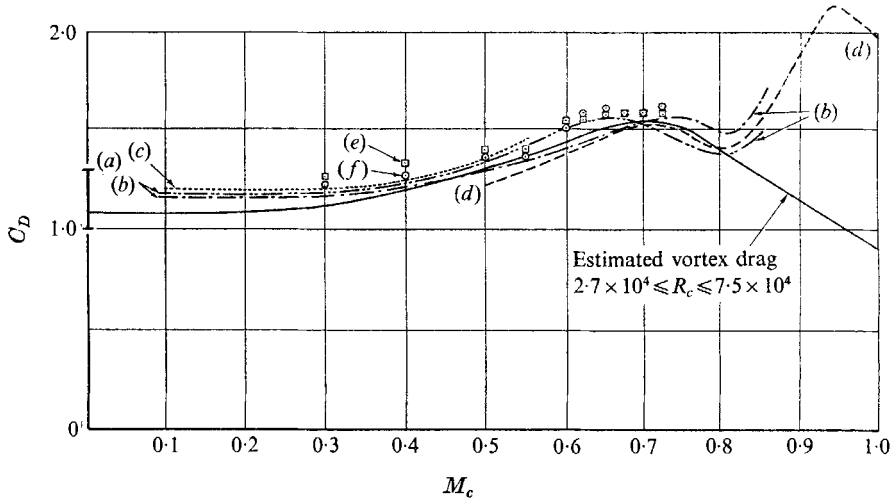

FIGURE 24. Drag of circular cylinders at subsonic speeds and subcritical Reynolds numbers. (*a*) Numerous experiments; $2{\cdot}7\times10^4 \leqslant R_c \leqslant 7{\cdot}5\times10^4$. Experimenters referred to by Thomson & Morrison (1965). (*b*) $2{\cdot}5\times10^4 \leqslant R_c \leqslant 1{\cdot}25\times10^5$ (?), Knowler & Pruden (1944). (*c*) $10^4 \leqslant R_c \leqslant 8\times10^4$, Lindsey (1938). (*d*) Fineness ratio 60. $1{\cdot}2\times10^5 \leqslant R_c \leqslant 3{\cdot}6\times10^5$, Welsh (1953), (*e*) $5{\cdot}1\times10^4 \leqslant R_c \leqslant 9{\cdot}4\times10^4$, Gowen & Perkins (1953). (*f*) $8{\cdot}5\times10^4 \leqslant R_c \leqslant 1{\cdot}57\times10^5$, Gowen & Perkins (1953).

the body near the nose, those remaining behave as if they are part of a yawed infinite vortex street. A combination of Kármán's vortex street theory and the sweepback principle enables the vortex strength to be deduced up to cross-flow Mach numbers of 1·0. At higher speeds the vortex street theory apparently becomes inadequate. For the cross-flow Mach number range 0–1·0 the vortex spacing ratio in the equivalent Kármán vortex street is nearly constant and approximately equal to 0·19. Both the strength and position of the first two or three vortices are dependent on the nose misalignment and are likely to vary for different wind tunnel models. However, the characteristics of later vortices are apparently independent of nose misalignments or nose shape.

Wake traverses show that considerable diffusion of vorticity occurs in the wake as the distance from the nose is increased and also as the Mach number increases although this is not readily apparent from schlieren studies. Schlieren photographs and their analysis using the Kármán vortex street theory have proved to be a very simple and powerful method for determining the Strouhal number, vortex paths and vortex strengths. This information when substituted into Kármán's expression for drag coefficient leads to a close estimate of the vortex drag of a two-dimensional circular cylinder at subsonic speeds.

REFERENCES

ABERNATHY, F. H. & KRONAUER, R. E. 1962 *J. Fluid Mech.* **13**, 1.

ALLEN, H. J. & PERKINS, E. W. 1951 *N.A.C.A. Rep.* 1048.

BIRKHOFF, G. & ZARANTONELLO, E. H. 1957 *Jets, Wakes and Cavities*, p. 284. Academic.

BURSNALL, W. S. & LOFTIN, L. K. 1951 *N.A.C.A. Tech. Note*, 2463.

DURAND, W. F. (ed.) 1935 *Aerodynamic Theory*, vol. 2, §E, VII, 342–349. Berlin: Springer.

FAGE, A. & JOHANSEN, F. C. 1927 *Proc. Roy. Soc.* A **116**, 170.

FIECHTER, M. 1966 *Deutsch-Französisches Forschungsinstitut Saint Louis*, Rep. 10/66.

FUNG, Y. C. 1960 *J. Aerospace Sci.* **27**, 801.

GASTER, M. 1969 *J. Fluid Mech.* **38**, 565.

GOLDSTEIN, S. (ed.) 1950 *Modern Developments in Fluid Dynamics*, p. 422. Oxford University Press.

GOWEN, F. E. & PERKINS, E. W. 1953 *N.A.C.A. Tech. Note*, 2960.

GRISS, R. J. 1967 *Australian A.R.L. Aerodynamic Tech.* Memo. 230.

HALL, I. M., ROGERS, E. W. E. & DAVIS, B. M. 1959 *Aero. Res. Coun. R. & M.* 3128.

HUMPHREYS, J. S. 1960 *J. Fluid Mech.* **9**, 603.

JORGENSEN, L. H. & PERKINS, E. W. 1958 *N.A.C.A. Rep.* 1371.

KNOWLER, A. E. & PRUDEN, F. W. 1944 *Aero. Res. Coun. R. & M.* 1933.

LINDSEY, W. F. 1938 *N.A.C.A. Rep.* 619.

MALTBY, R. L. & PECKHAM, D. H. 1956 *R.A.E. Tech. Note Aero.* 2482.

MELLO, J. F. 1959 *J. Aerospace Sci.* **26**, 155.

MORKOVIN, M. V. 1964 Symposium on fully separated flows. *A.S.M.E.* 102.

NAUMANN, A., MORSBACH, M. & KRAMER, C. 1966 Separated flows. *Agard C.P.* no. 4, 539.

SARPKAYA, T. 1966 *A.I.A.A. J.* **4**, 414.

SCHLICHTING, H. 1968 *Boundary Layer Theory*, 6th edn. pp. 238–240. McGraw-Hill.

THOMSON, K. D. 1970 *Aeronaut. J. Roy. Aero. Soc.* **74**, 762.

THOMSON, K. D. & MORRISON, D. F. 1965 *Australian W.R.E. Tech. Note*, HSA 106.

THOMSON, K. D. & MORRISON, D. F. 1969 *Australian W.R.E. Rep.* HSA 25.

WELSH, C. J. 1953 *N.A.C.A. Tech. Note*, 2941.

WILLE, R. 1966 *Progress in Aeronautical Sciences*, vol. 7, p. 195. Pergamon.

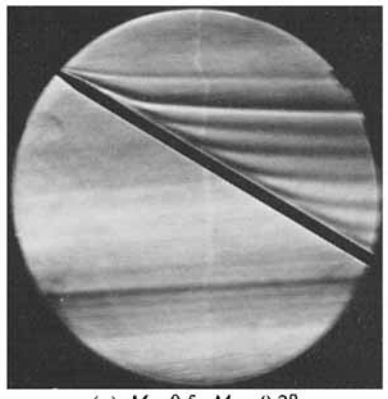

(*a*) $M=0{\cdot}5$, $M_c=0{\cdot}28$

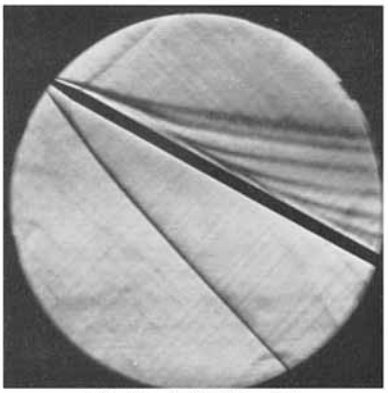

(*b*) $M=1{\cdot}40$, $M_c=0{\cdot}7$

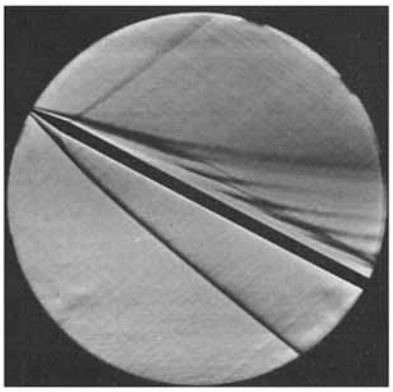

(*c*) $M=1{\cdot}6$, $M_c=0{\cdot}8$

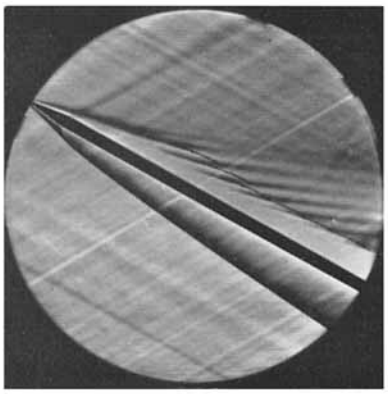

(*d*) $M=2{\cdot}0$, $M_c=1{\cdot}0$

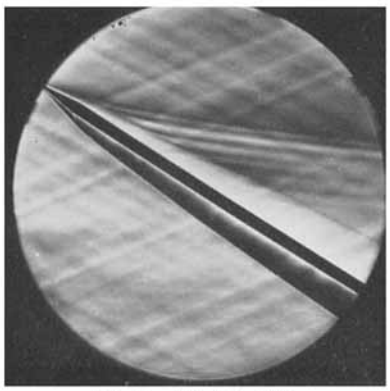

(*e*) $M=2{\cdot}4$, $M_c=1{\cdot}2$

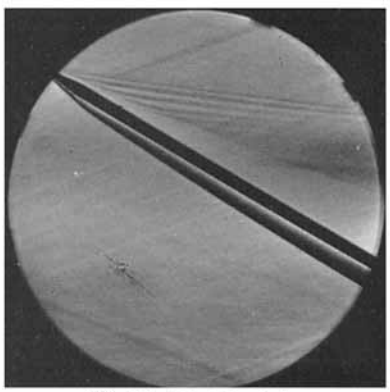

(*f*) $M=2{\cdot}8$, $M_c=1{\cdot}4$

FIGURE 2. Variation in wake pattern with Mach number at approximately 30° incidence.

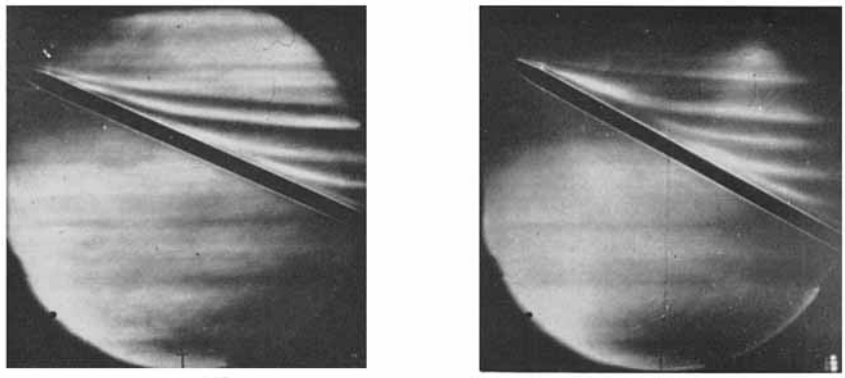

(*a*) $\alpha = 25°$ (*b*) $\alpha = 30°$

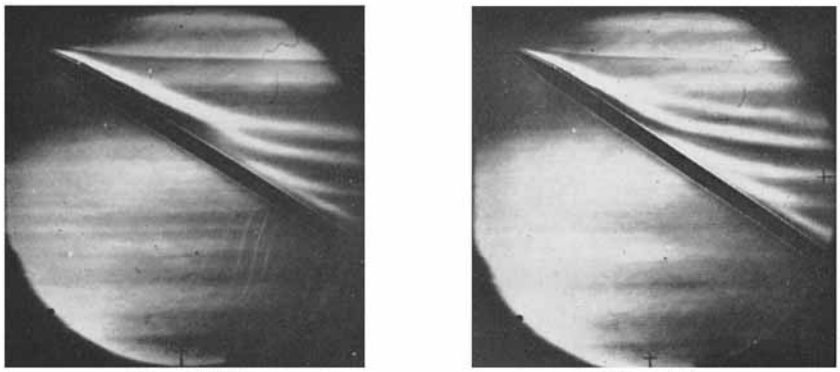

(*c*) $\alpha = 33{\cdot}2°$ (*d*) $\alpha = 35°$

(*e*) $\alpha = 40°$

FIGURE 3. Variation in wake pattern with incidence at $M = 0{\cdot}8$. $R_c = 0{\cdot}71 \times 10^5 \sin\alpha$.

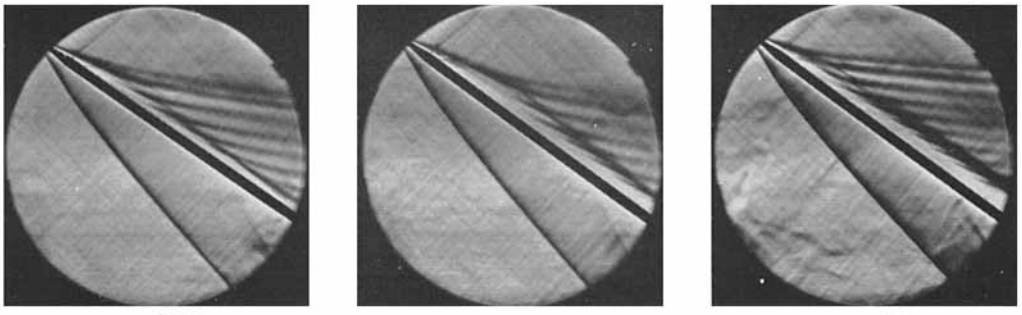

FIGURE 4. Variation in wake pattern with incidence at $M = 1{\cdot}4$. $R_c = 0{\cdot}90 \times 10^5 \sin \alpha$.

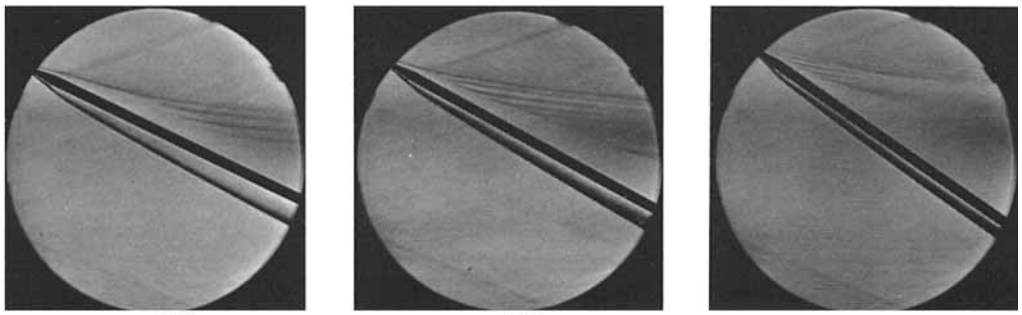

FIGURE 5. Variation in wake pattern with incidence at $M = 2{\cdot}8$. $R_c = 1{\cdot}12 \times 10^5 \sin \alpha$.

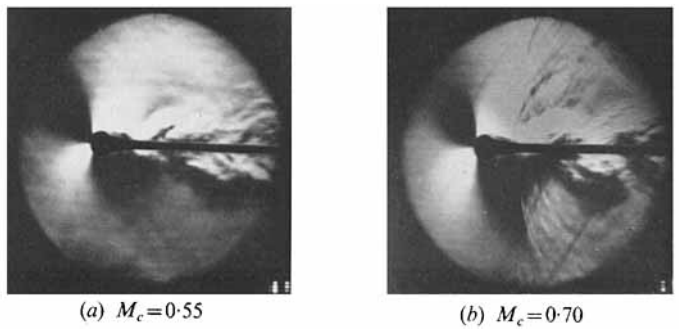

FIGURE 6. Wake from a two-dimensional circular cylinder at subsonic speeds. $R_c \approx 10^5$.